

Article

2D and 3D Visualization for the Static Bifurcations and Nonlinear Oscillations of a Self-Excited System with Time-Delayed Controller

Nasser A. Saeed ^{1,*} , Jan Awrejcewicz ² , Mohamed A. Alkashif ³  and Mohamed S. Mohamed ⁴ 

¹ Department of Physics and Engineering Mathematics, Faculty of Electronic Engineering, Menoufia University, Menouf 32952, Egypt

² Department of Automation, Biomechanics, and Mechatronics, Faculty of Mechanical Engineering, Lodz University of Technology, 90924 Lodz, Poland; jan.awrejcewicz@p.lodz.pl

³ Department of Science and Technology, University College—Ranyah, Taif University, P.O. Box 11099, Taif 21944, Saudi Arabia; m.alkashif@tu.edu.sa

⁴ Department of Mathematics and Statistics, College of Science, Taif University, P.O. Box 11099, Taif 21944, Saudi Arabia; m.saaad@tu.edu.sa

* Correspondence: nasser.a.saeed@el-eng.menofia.edu.eg

Abstract: This research focuses on the nonlinear vibration control of a self-excited single-degree-of-freedom system. The integral resonant controller (IRC) is introduced to stabilize the unstable motion and suppress nonlinear oscillations of the considered system. The nonlinear dynamical equations that govern the vibratory behaviors of the proposed closed-loop control system are investigated using perturbation analysis, where loop delays have been included in the studied model. The system bifurcation behaviors have been visualized in both the two and three-dimensional spaces, and corresponding dynamical behaviors have been explored numerically using the bifurcation diagrams, Poincaré map, time-response, zero-one chaotic test algorithm, and frequency spectrum. The obtained analytical investigations revealed that the uncontrolled system can oscillate with one of four vibration modes depending on the excitation frequency, which are mono-stable periodic motion, bi-stable periodic motion, periodic and quasi-period motion, and quasi-periodic motion only. In addition, it is found that the existence of time delays in the control loop can either improve or degrade the control performance. Therefore, an objective function has been introduced to design the optimum control parameters. Based on the derived objective function, it is found that the performance of the proposed control strategy is proportional to the product of the control and feedback gains and inversely proportional to the internal loop feedback gain when the loop delays are neglected. Moreover, it is reported that the controller performance is a periodic function of the total sum of the loop delays. Accordingly, the optimal operating conditions of the time-delayed integral resonant controller have been explained. Finally, numerical validations for all obtained analytical results have been performed, where an excellent correspondence between the analytical and numerical investigations has been demonstrated.

Keywords: time delay; self-excited system; stability chart; static bifurcation; periodic and quasi-periodic oscillations; bifurcation diagrams; zero-one chaotic test; Poincaré map and frequency spectrum



Citation: Saeed, N.A.; Awrejcewicz, J.; Alkashif, M.A.; Mohamed, M.S. 2D and 3D Visualization for the Static Bifurcations and Nonlinear Oscillations of a Self-Excited System with Time-Delayed Controller. *Symmetry* **2022**, *14*, 621. <https://doi.org/10.3390/sym14030621>

Academic Editors: Antonio Palacios and Young S. Kim

Received: 12 February 2022

Accepted: 18 March 2022

Published: 20 March 2022

Publisher's Note: MDPI stays neutral with regard to jurisdictional claims in published maps and institutional affiliations.



Copyright: © 2022 by the authors. Licensee MDPI, Basel, Switzerland. This article is an open access article distributed under the terms and conditions of the Creative Commons Attribution (CC BY) license (<https://creativecommons.org/licenses/by/4.0/>).

1. Introduction

Self-excited oscillations arise in many nonlinear dynamical systems mainly due to the existence of negative damping or cross-coupling stiffness, where this type of oscillations may occur even in the absence of external excitation forces. Basically, the self-excited vibrations are caused by a particular type of nonlinear excitation force. This type of exciting force has the feature of increasing the excitation amplitude for small velocities and decreasing the excitation amplitude for large velocities of the vibrating system [1]. According to this excitation mechanism, a periodic vibratory motion will be built up even if the external forces

are negligible [2]. In real life, the flowing of the wind or the fluids with constant velocity can cause self-exciting oscillations for the engineering structures. In addition, the relative dry-friction oscillator is a well-known example of a self-excited system in mechanical engineering. In literature, the self-excitation mechanism has been modeled mathematically as a nonlinear damping coefficient that causes self-excited oscillations, where two common models have been introduced. The first model is namely the van der Pol model that defined by the nonlinear function $f_V = (-\mu_V \dot{x} + \beta_V x^2 \dot{x})$, while the second model is namely the Rayleigh model that defined by $f_R = (-\mu_R \dot{x} + \beta_R \dot{x}^3)$. Despite the two introduced models seeming to be different, Warminski [3] proved that the van der Pol and Rayleigh models can be treated as equivalent to each other. The self-excited oscillations sometimes have catastrophic effects on some engineering structures, where the breakdown of the Tacoma bridge has been done due to heavy self-excited vibrations caused by a constant velocity air storm in 1940 (see Tondl et al. [4] for more examples). Therefore, investigating and suppressing these undesirable oscillations was and still is one of the main subjects of researchers and engineers worldwide, where Szabelski and Warminski [5,6] studied the steady-state oscillatory motions of the well-known self-excited Duffing oscillator subjected to both inertial and parametric excitations. The authors reported that the parametric and inertial excitations have a significant influence on the system bifurcation behaviors, where five simultaneous solutions have been found. Szabelski and Warminski [7] investigated the nonlinear oscillations of a self-excited two-degree-of-freedom system subjected to both parametric and external excitations. The authors concluded that the coexistence of both parametric and external excitations results in the appearance of multi-stable solutions at a specific frequency band of the excitation force. On the other hand, many control strategies have been introduced to control the self-excited oscillations of different dynamical systems [8–10]. El-Budway and Nasr El-Deen [8] used the saturation-based control strategy to mitigate the nonlinear vibration of a self-excited van der Pol oscillator. The authors reported that the applied control algorithm may reduce the system oscillation to some level, but the controller robustness has not been emphasized. Jun et al. [9] employed the saturation-based control technique to control the free oscillations of a self-excited system. The authors concluded that the applied control strategy can mitigate the system oscillations to some extent. However, the obtained results showed that the controller efficiency is not feasible. Warminski et al. [10] introduced the saturation controller to control the nonlinear oscillation of an externally excited self-excited system. They concluded that the introduced control algorithm can suppress the system vibrations with high efficiency when tuning the controller's natural frequency to one-half of the system's natural frequency. However, the suggested control method has been failed to stabilize the unstable behaviors of the studied self-excited system. Abdelhafez and Nassar [11] introduced the positive-position feedback control algorithm to suppress the nonlinear oscillations of a harmonically self-excited system. They considered the time delays in the studied model. Based on the presented analysis, the authors reported that the introduced controller can control the system oscillatory behaviors with high performance when the loop delays are neglected. In addition, the authors showed that the existence of the time delays in the control loop may degrade the control efficiency and destabilize the controlled system.

Time delay is an essential phenomenon in every active control system, which arises due to control components such as the sensors, actuators, and digital controllers. Therefore, the influence of the time delays on the control performance and stability conditions has been extensively investigated in many control systems [12–25], where Macarri [12] used a time-delayed linear position-velocity controller to study nonlinear vibration control of a cantilever beam system. Alhazza et al. [13,14] and Ping et al. [15] explored the control efficiency of the time-delayed position, time-delayed velocity, and time-delayed acceleration controllers in suppressing the multimode transversal vibrations of a cantilever beam. The influence of time delay on the vibration control efficiency of both the linear and cubic nonlinear forms of position, velocity, and acceleration feedback controllers was discussed by Daqaq et al. [16]. Zhao and Xu [17] studied the influence of the time-delayed position

feedback control on the oscillatory behaviors of an auto-parametric vibration absorber. Based on the obtained results regarding references [12–17], the main conclusion is that the existence of time delays may result in either improving or destabilizing the system under control depending on the magnitudes of the loop delays. Saeed et al. [18,19] introduced both linear and nonlinear versions of the time-delayed position-velocity controller to mitigate the nonlinear lateral vibration in rotating machinery. Saeed et al. [20,21] studied the effect of the time delays on the vibration suppression efficiency of both the linear and cubic nonlinear forms of the position, velocity, and acceleration controllers. Based on the introduced discussions in references [18–21], The authors proved that the time delays can be used according to a defined optimization function to enhance the controller performance rather than destabilizing the system under control. In addition, the influence of the time delays on the efficiency of some advanced control algorithms such as nonlinear saturation and positive-position controllers has been discussed [22–25], where the obtained results showed the existence of loop delays always has an undesirable effect on both the control efficiency and system stability.

Integral resonant controller (IRC) has been introduced before to enhance the nonlinear vibratory characteristics of many engineering systems [26–33], where the IRC is applied to control the oscillatory behaviors of light-weight engineering structures [26]. Al-Mamun et al. [27] investigated the IRC's control performance in mitigating nonlinear vibrations of a piezoelectric micro-actuator system. Omidi and Mahmoodi [28–30] employed the IRC to improve the positive-position feedback controller efficiency. MacLean and Sumeet [31] used the IRC to eliminate motion bifurcation and mitigate the nonlinear vibrations of a micro-cantilever beam system. Saeed et al. [32] applied a nonlinear version of the time-delayed integral resonant controller to suppress the nonlinear vibrations of a parametrically excited system. The authors reported that loop delays can be designed according to a defined optimization function either to improve or degrade the controller performance. In addition, they showed that the optimized controller can eliminate the system transversal oscillations to zero. Recently, Saeed et al. [33] used the IRC along with the linear PD-controller to reduce the nonlinear lateral vibrations of an eight-pole active magnetic bearings system, where the obtained results demonstrated the feasibility of the IRC in eliminating the system's catastrophic nonlinear bifurcations.

Despite many control algorithms such as the saturation-based control [8–10] and positive-position feedback control [11] have introduced to control the nonlinear motion of various self-excited systems, the integral resonant controller has not been applied before to control the dynamical characteristics of such systems. Accordingly, the integral resonant controller is introduced within this article to improve the oscillatory behaviors and stabilize the unstable motion of a self-excited system for the first time. The nonlinear differential equations that govern the dynamical behaviors of both the self-excited system and proposed controller are obtained, where the loop delays have been included in the studied model. By applying the multiple time-scales perturbation technique, the slow-flow amplitude-phase modulation equations are derived. Then, the corresponding frequency-response equation is extracted. According to the obtained frequency-response equation, the motion bifurcations have been investigated in the two- and three-dimensional spaces. The efficiency of the suggested control algorithm in mitigating the nonlinear oscillation and stabilizing unstable motion of the considered system has been explored. The obtained results demonstrated the feasibility of the applied control strategy in both eliminating the nonlinear vibrations and stabilizing the unstable motion considered system. In addition, it is reported that the loop delays can be used to improve the controller efficiency rather than degrading it according to a defined optimization function. Finally, numerical validations for all obtained results have been performed using the OD45 and DDE 23 MATLAB solvers, where the numerical simulations confirmed the accuracy of the acquired analytical results.

2. Mathematical Model and Frequency-Response Equation

2.1. Mathematical Model

A cantilever beam system of length L , width b , thickness h , and a lumped mass M attached to its end is shown in Figure 1. The beam system is mounted on a metallic base that is excited periodically along the X -axis using an electrical shaker. The nonlinear mathematical model that governs beam system first-mode transversal oscillation can be expressed as follows [10,11,34]:

$$\ddot{x} + (-\mu\dot{x} + \beta\dot{x}^3) + \omega^2x + \alpha x^3 + \gamma(x\dot{x}^2 + x^2\ddot{x}) = f\lambda\Omega^2 \cos(\Omega t) + U \tag{1}$$

where $(-\mu\dot{x} + \beta\dot{x}^3)$ represents the Rayleigh nonlinear damping term due to the air-flow with constant velocity as shown in Figure 1 (see references [1–4]), and U is the suggested control force to stabilize the unstable motion of the cantilever beam system.

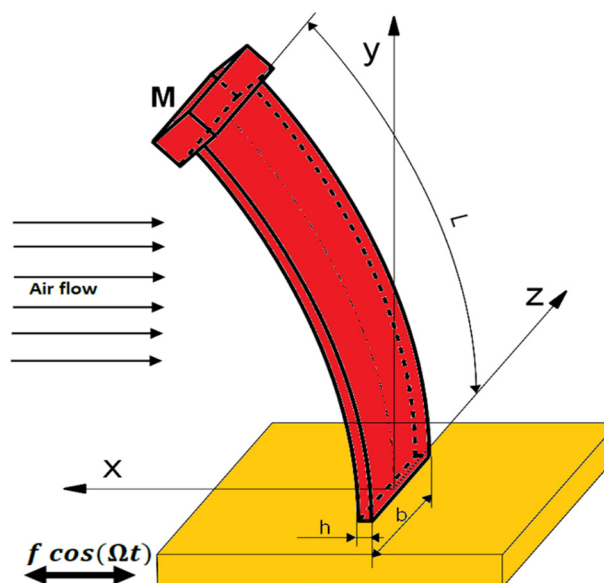


Figure 1. Cantilever beam system with both external and self-excitation.

Within this work, the time-delayed integral resonant controller (TDIRC) has been proposed to suppress the transversal oscillations and stabilize the unstable motions of the considered self-excited system. Accordingly, the equation motion given by Equation (1) can be rewritten as follows [26–33]:

$$\ddot{x} - \mu\dot{x} + \omega^2x + \alpha x^3 + \beta\dot{x}^3 + \gamma(x\dot{x}^2 + x^2\ddot{x}) = f\lambda\Omega^2 \cos(\Omega t) + \delta_1 y(t - \tau_1) \tag{2}$$

$$\dot{y} + \eta y = \delta_2 x(t - \tau_2) \tag{3}$$

The control force U in Equation (1) is selected to be $U = \delta_1 y(t - \tau_1)$, where δ_1 is the control signal gain, $y(t - \tau_1)$ is the control signal that is generated via the integral resonant controller, and τ_1 denotes the control signal time delay that arises due to the signal processing time. The dynamics of the integral resonant controller is governed by a second-order differential equation (i.e., Equation (3)) that is coupled to the self-excited system via the feedback gain δ_2 . Figure 2 shows the engineering implementation of the proposed control algorithm in detail, where Figure 2a illustrates the self-excited cantilever beam system that is equipped with both MFC sensor and MFC actuator, where the abbreviation MFC stands for macro fiber composite smart material used as sensors and actuator to control the nonlinear oscillations of the continuous dynamical system [35]. The sequential execution of the suggested control method is depicted in Figure 2b, where the MFC sensor measures the transversal oscillation of the considered beam system $x(t)$. The measured

signal $x(t)$ is fed into a digital controller via an analog-to-digital converter. The acquired signal is then manipulated according to the proposed TDIRC control law to compute the control signal $y(t - \tau_1)$ that is amplified via a power amplifier to become to $\delta_1 y(t - \tau_1)$. Finally, the manipulated control signal is applied via MFC actuator to mitigate the nonlinear oscillations of the self-excited system.

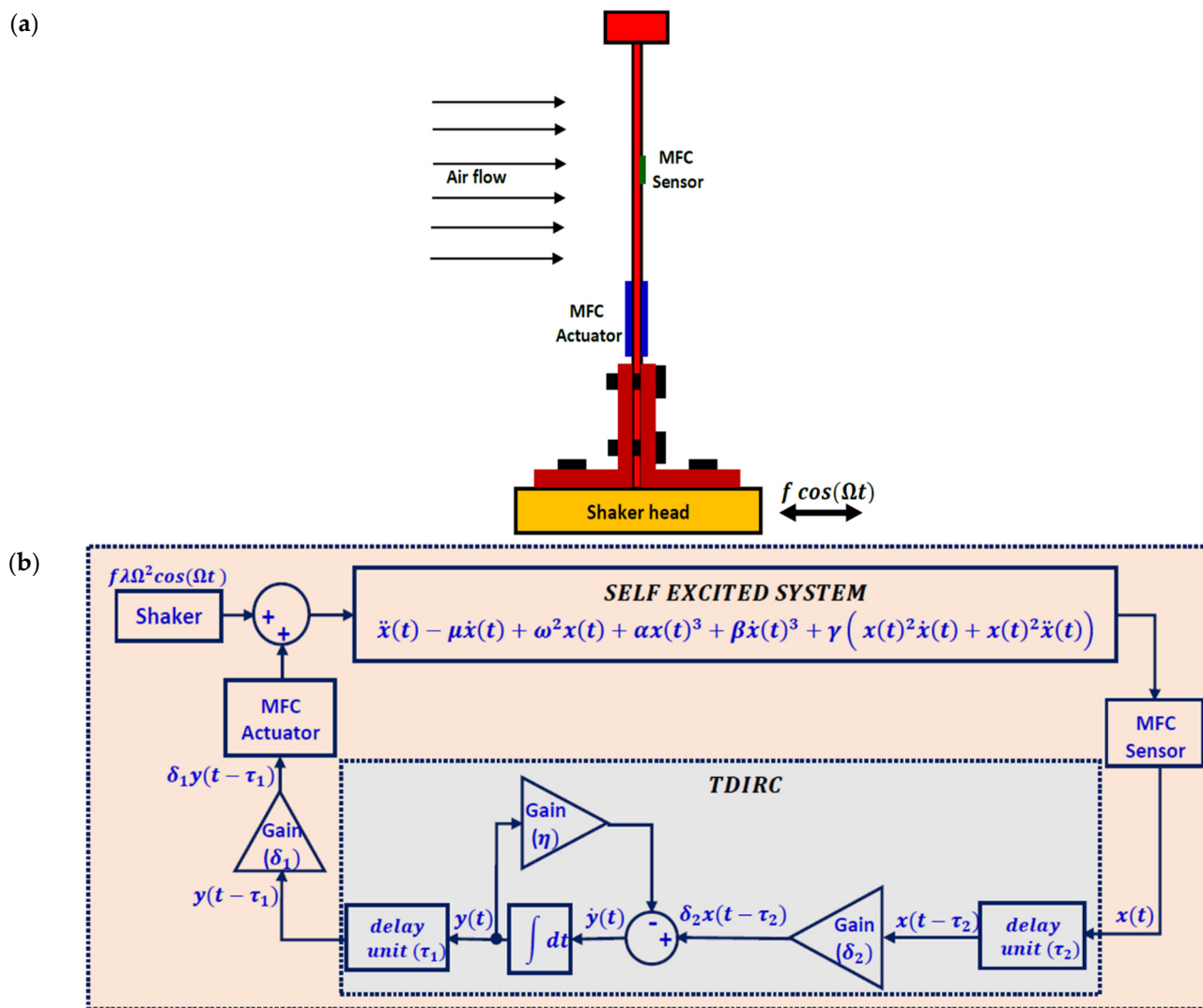


Figure 2. (a) The self-excited cantilever beam system equipped with an electrical shaker, MFC sensor, and MFC actuator, and (b) schematic diagram of the self-excited system coupled to TDIRC.

To report the optimum control parameters (i.e., $\delta_1, \delta_2, \eta, \tau_1, \tau_2$) that can be employed to stabilize the unstable motion and reduce the transversal oscillation of the targeted self-excited system, it is required to obtain an analytical solution to Equations (2) and (3). Accordingly, the perturbation analysis is employed to find an approximated solution to the considered time-delayed nonlinear system as given in Section 2.2.

2.2. Frequency-Response Equation

An approximate analytical solution to the time-delayed dynamical system given by Equations (2) and (3) can be sought using the multiple time-scales perturbation method as follows [36,37]:

$$x(t, \epsilon) = x_0(T_0, T_1) + \epsilon x_1(T_0, T_1) + O(\epsilon^2), \tag{4}$$

$$y(t, \epsilon) = \epsilon y_0(T_0, T_1) + \epsilon^2 y_1(T_0, T_1) + O(\epsilon^3) \tag{5}$$

where ε is the well-known perturbation parameter, $T_0 = t$ and $T_1 = \varepsilon t$ denote the fast and slow time scales that are used to capture the fast and slow dynamical motions of the considered closed-loop control system. Accordingly, the time-delayed solution can be expressed as follows:

$$x(t - \tau_2, \varepsilon) = x_{0\tau_2}(T_0 - \tau_2, T_1 - \varepsilon\tau_2) + \varepsilon x_{1\tau_2}(T_0 - \tau_2, T_1 - \varepsilon\tau_2) + O(\varepsilon^2), \tag{6}$$

$$y(t - \tau_1, \varepsilon) = \varepsilon y_{0\tau_1}(T_0 - \tau_1, T_1 - \varepsilon\tau_1) + \varepsilon^2 y_{1\tau_1}(T_0 - \tau_1, T_1 - \varepsilon\tau_1) + O(\varepsilon^3) \tag{7}$$

According to the introduced time scales T_0 and T_1 , the ordinary derivatives $\frac{d}{dt}$ and $\frac{d^2}{dt^2}$ can be rewritten in terms of T_0 and T_1 as follows:

$$\frac{d}{dt} = \frac{\partial}{\partial T_0} + \varepsilon \frac{\partial}{\partial T_1}, \quad \frac{d^2}{dt^2} = \frac{\partial^2}{\partial T_0^2} + 2\varepsilon \frac{\partial^2}{\partial T_0 \partial T_1} + O(\varepsilon^2). \tag{8}$$

To apply the multiple scales procedure, the system and control parameters may be scaled as follows:

$$\mu = \varepsilon \hat{\mu}, \quad \alpha = \varepsilon \hat{\alpha}, \quad \beta = \varepsilon \hat{\beta}, \quad \gamma = \varepsilon \hat{\gamma}, \quad \delta_2 = \varepsilon \hat{\delta}_2, \quad f = \varepsilon \hat{f} \tag{9}$$

Substituting Equations (4)–(9) into Equations (2) and (3), with equating the coefficients of the same power of ε , we get:

$$O(\varepsilon^0): \left(\frac{\partial^2}{\partial T_0^2} + \omega^2 \right) x_0 = 0 \tag{10}$$

$$O(\varepsilon^1): \left(\frac{\partial}{\partial T_0} + \eta \right) y_0 = \hat{\delta}_2 x_{0\tau_2} \tag{11}$$

$$\left(\frac{\partial^2}{\partial T_0^2} + \omega^2 \right) x_1 = -2 \frac{\partial^2 x_0}{\partial T_0 \partial T_1} + \hat{\mu} \frac{\partial x_0}{\partial T_0} - \hat{\alpha} x_0^3 - \hat{\beta} \left(\frac{\partial x_0}{\partial T_0} \right)^3 - \hat{\gamma} x_0 \left(\frac{\partial x_0}{\partial T_0} \right)^2 - \hat{\gamma} x_0^2 \left(\frac{\partial^2 x_0}{\partial T_0^2} \right) + \delta_1 y_{0\tau_1} + \hat{f} \lambda \Omega^2 \cos(\Omega T_0) \tag{12}$$

The solution of the homogeneous differential equation given by Equation (10) can be expressed as follows:

$$x_0(T_0, T_1) = A(T_1) e^{i\omega T_0} + \bar{A}(T_1) e^{-i\omega T_0} \tag{13}$$

where $A(T_1)$ is an unknown function that will be determined with the next solution steps. Accordingly, the time-delayed solution $x_{0\tau_2}(T_0 - \tau_2, T_1 - \varepsilon\tau_2)$ can be expressed as follows:

$$x_{0\tau_2}(T_0, -\tau_2, T_1 - \varepsilon\tau_2) = A(T_1 - \varepsilon\tau_2) e^{i\omega(T_0 - \tau_2)} + \bar{A}(T_1 - \varepsilon\tau_2) e^{-i\omega(T_0 - \tau_2)} \tag{14}$$

Expanding the function $A(T_1 - \varepsilon\tau_k)$, $k = 1, 2$ into Maclaurin series assuming $\varepsilon\tau_k \ll 1$ and $\varepsilon^2\tau_k \ll 1$ [17–22], we have

$$A(T_1 - \varepsilon\tau_k) = A(T_1) - \varepsilon\tau_k D_1 A(T_1) - \varepsilon^2\tau_k D_2 A(T_1) + \dots \cong A(T_1), \quad k = 1, 2. \tag{15}$$

According to Equations (14) and (15), the time-delayed solution $x_{0\tau_2}(T_0 - \tau_2, T_1 - \varepsilon\tau_2)$ can be approximated as follows:

$$x_{0\tau_2}(T_0 - \tau_2, T_1 - \varepsilon\tau_2) = A(T_1) e^{i\omega(T_0 - \tau_2)} + \bar{A}(T_1) e^{-i\omega(T_0 - \tau_2)} \tag{16}$$

Substituting Equation (16) into the right-hand side of Equation (11), with solving the corresponding nonhomogeneous differential equation, we have the following steady-state solution

$$y_0(T_0, T_1) = \frac{\eta - i\omega}{\eta^2 + \omega^2} \delta_2 A(T_1) e^{i\omega(T_0 - \tau_2)} + \frac{\eta + i\omega}{\eta^2 + \omega^2} \delta_2 \bar{A}(T_1) e^{-i\omega(T_0 - \tau_2)} \tag{17}$$

Based on Equation (17), the time-delayed solution $y_{0\tau_1}(T_0 - \tau_1, T_1 - \varepsilon\tau_1)$ can be expressed so that:

$$y_{0\tau_1}(T_0 - \tau_1, T_1 - \varepsilon\tau_1) = \frac{\eta - i\omega}{\eta^2 + \omega^2} \delta_2 A(T_1) e^{i\omega(T_0 - \tau_1 - \tau_2)} + \frac{\eta + i\omega}{\eta^2 + \omega^2} \delta_2 \bar{A}(T_1) e^{-i\omega(T_0 - \tau_1 - \tau_2)} \tag{18}$$

Substituting Equations (13) and (18) into Equation (12), we have

$$\begin{aligned} \left(\frac{\partial^2}{\partial T_0^2} + \omega^2\right) x_1 &= \left(-2i\omega \frac{\partial A}{\partial T_1} + i\omega \hat{\mu} A - 3\hat{\alpha} A^2 \bar{A} - 3i\omega^3 \hat{\beta} A^2 \bar{A} + 2\omega^2 \hat{\gamma} A^2 \bar{A} \right. \\ &\quad \left. + \frac{\eta - i\omega}{\eta^2 + \omega^2} \delta_1 \delta_2 A e^{-i\omega(\tau_1 + \tau_2)}\right) e^{i\omega T_0} - (\hat{\alpha} A^3 + i\omega^3 \hat{\beta} A^3 + 2\omega^2 \hat{\gamma} A^3) e^{3i\omega T_0} \\ &\quad + \frac{1}{2} \hat{f} \lambda \Omega^2 e^{i\Omega T_0} + cc \end{aligned} \tag{19}$$

where cc denotes the complex conjugate terms. To investigate the dynamical behaviors of the controlled self-excited system at the primary resonance case (i.e., when Ω is close to ω), let the detuning parameter σ represents the closeness of Ω to ω as follows:

$$\Omega = \omega + \sigma \tag{20}$$

Substituting Equation (20) into Equation (19), one can deduce the following solvability condition of Equation (19):

$$\begin{aligned} -2i\omega \frac{\partial A}{\partial T_1} + i\omega \hat{\mu} A - 3\hat{\alpha} A^2 \bar{A} - 3i\omega^3 \hat{\beta} A^2 \bar{A} + 2\omega^2 \hat{\gamma} A^2 \bar{A} + \frac{\eta - i\omega}{\eta^2 + \omega^2} \delta_1 \delta_2 A e^{-i\omega(\tau_1 + \tau_2)} \\ + \frac{1}{2} \hat{f} \lambda (\omega + \sigma)^2 e^{i\sigma T_0} = 0 \end{aligned} \tag{21}$$

Now, by returning each scaled parameter in Equation (21) to its original form (i.e., $T_1 = \varepsilon t$, $\hat{\mu} = \frac{\mu}{\varepsilon}$, $\hat{\alpha} = \frac{\alpha}{\varepsilon}$, $\hat{\beta} = \frac{\beta}{\varepsilon}$, $\hat{\gamma} = \frac{\gamma}{\varepsilon}$, $\hat{\delta}_2 = \frac{\delta_2}{\varepsilon}$, $\hat{f} = \frac{f}{\varepsilon}$), we have

$$\begin{aligned} -2i\omega \frac{dA}{dt} + i\omega \mu A - 3\alpha A^2 \bar{A} - 3i\omega^3 \beta A^2 \bar{A} + 2\omega^2 \gamma A^2 \bar{A} + \frac{\eta - i\omega}{\eta^2 + \omega^2} \delta_1 \delta_2 A e^{-i\omega(\tau_1 + \tau_2)} \\ + \frac{1}{2} f \lambda (\omega + \sigma)^2 e^{i\sigma T_0} = 0 \end{aligned} \tag{22}$$

To investigate Equation (22), it is convenient to express the unknown function $A(t)$ in polar for as follows [36,37]:

$$A(t) = \frac{1}{2} a(t) e^{i\theta(t)}, \quad \frac{dA}{dt} = \frac{1}{2} \dot{a}(t) e^{i\theta(t)} + \frac{1}{2} i a(t) \dot{\theta}(t) e^{i\theta(t)} \tag{23}$$

Substituting Equation (23) into Equation (22) and then separating the real and imaginary parts, we can obtain the following slow-flow modulating equations.

$$\begin{aligned} \dot{a}(t) &= -\frac{1}{2} \left[-\mu + \frac{\delta_1 \delta_2}{(\eta^2 + \omega^2)} \cos(\omega\tau_1 + \omega\tau_2) + \frac{\eta \delta_1 \delta_2}{\omega(\eta^2 + \omega^2)} \sin(\omega\tau_1 + \omega\tau_2) \right] a(t) - \frac{3}{8} \beta \omega^2 a^3(t) \\ &\quad + \frac{f\lambda}{2\omega} (\omega + \sigma)^2 \sin(\phi(t)) \end{aligned} \tag{24}$$

$$\begin{aligned} \dot{\phi}(t) &= \left[\sigma - \frac{\delta_1 \delta_2}{2(\eta^2 + \omega^2)} \sin(\omega\tau_1 + \omega\tau_2) + \frac{\eta \delta_1 \delta_2}{2\omega(\eta^2 + \omega^2)} \cos(\omega\tau_1 + \omega\tau_2) \right] - \frac{1}{4} \left[\frac{3\alpha}{2\omega} - \gamma \omega \right] a^2(t) \\ &\quad + \frac{f\lambda}{2\omega a(t)} (\omega + \sigma)^2 \cos(\phi(t)) \end{aligned} \tag{25}$$

where $\phi(t) = \sigma t - \theta(t)$. Now, by substituting Equations (13), (17), and (23) into Equations (4) and (5) considering Equation (20), we get the proposed approximate solution of Equations (2) and (3) as follows:

$$x(t) = a(t) \cos(\Omega t - \phi(t)) \tag{26}$$

$$y(t) = \frac{\delta_2}{\eta^2 + \omega^2} a(t) [\eta \cos(\Omega t - \phi(t) - \omega \tau_2) + \omega \sin(\Omega t - \phi(t) - \omega \tau_2)] \tag{27}$$

Based on Equation (26), $a(t)$ denotes the oscillation amplitude of the controlled self-excited system, and $\phi(t)$ is the phase angle of the system motion. At steady-state, we can write $\dot{a}(t) = \dot{\phi}(t) = 0.0$. Substituting $\dot{a}(t) = \dot{\phi}(t) = 0$ into Equations (24) and (25) with eliminating $\phi(t)$, one can obtain the following frequency-response equation.

$$\left[\mu a - \frac{\delta_1 \delta_2}{(\eta^2 + \omega^2)} \cos(\omega \tau_1 + \omega \tau_2) a - \frac{\eta \delta_1 \delta_2}{\omega(\eta^2 + \omega^2)} \sin(\omega \tau_1 + \omega \tau_2) a - \frac{3}{4} \beta \omega^2 a^3 \right] + \left[2\sigma - \frac{3}{8} \alpha a^2 + \frac{1}{2} \gamma \omega a^2 + \frac{\eta \delta_1 \delta_2}{\omega(\eta^2 + \omega^2)} \cos(\omega \tau_1 + \omega \tau_2) - \frac{\delta_1 \delta_2}{(\eta^2 + \omega^2)} \sin(\omega \tau_1 + \omega \tau_2) \right] = \left(1 + \frac{1}{a^2} \right) \frac{(\omega + \sigma)^4 f^2 \lambda^2}{\omega^2} \tag{28}$$

Equation (28) governs the relationship between the oscillation amplitude (a) of the controlled self-excited system and the different control parameters (i.e., $\delta_1, \delta_2, \eta, \tau_1$, and τ_2). So, solving this nonlinear algebraic equation using a as a function of the system and control parameters ($\sigma, f, \delta_1, \delta_2, \eta, \tau_1, \tau_2$), one can explore the influence of the different controller parameters on the steady-state vibration amplitude of the considered system, as illustrated in the following section. In addition, to study the solution stability of Equation (28), one can check the eigenvalues of the corresponding linearized system of Equations (24) and (25). Therefore, let the steady-state solution of Equations (24) and (25) is (a_0, ϕ_0) and consider (a_1, ϕ_1) be a small deviation about this steady-state solution. Accordingly, we can write

$$a = a_1 + a_0, \phi = \phi_1 + \phi_0, \dot{a} = \dot{a}_1, \dot{\phi} = \dot{\phi}_1 \tag{29}$$

Substituting Equation (29) into Equations (24) and (25), one can obtain the corresponding linearized system of Equations (24) and (25) about the equilibrium point (a_0, ϕ_0) as follows:

$$\begin{bmatrix} \dot{a}_1 \\ \dot{\phi}_1 \end{bmatrix} = \begin{bmatrix} J_{11} & J_{12} \\ J_{21} & J_{22} \end{bmatrix} \begin{bmatrix} a_1 \\ \phi_1 \end{bmatrix} \tag{30}$$

where $J_{11} = \frac{1}{2} \left[\mu - \frac{\delta_1 \delta_2}{\eta^2 + \omega^2} \cos(\omega \tau_1 + \omega \tau_2) - \frac{\eta \delta_1 \delta_2}{\omega(\eta^2 + \omega^2)} \sin(\omega \tau_1 + \omega \tau_2) \right] - \frac{9}{8} \beta \omega^2 a_0^2$, $J_{12} = \frac{f \lambda}{2 \omega} (\omega + \sigma)^2 \cos(\phi_0)$, $J_{21} = -\frac{3 \alpha a_0}{4 \omega} + \frac{1}{2} \gamma \omega a_0 - \frac{f \lambda}{2 a_0^2 \omega} (\omega + \sigma)^2 \cos(\phi_0)$, $J_{22} = -\frac{f \lambda}{2 a_0 \omega} (\omega + \sigma)^2 \sin(\phi_0)$. Accordingly, the solution stability of Equation (29) can be checked via investigating the eigenvalues of the linear dynamical system given by Equation (30) (see reference [38]).

3. Results and Discussion

According to the mathematical investigations given in Section 2, one can explore the effect of the different system and control parameters on the oscillation amplitude (a) of the considered self-excited system via solving Equation (28) as a function of one or two parameters with fixing the other parameters constant. In addition, the stability of Equation (28) solution can be checked by investigating the eigenvalues of the linear dynamical system given by Equation (30). It is considered that the studied cantilever beam system is made of glass-epoxy composite material with the physical coefficients: beam length $L = 23.6$ cm, beam width $b = 1.28$ cm, beam thickness $h = 0.1$ cm, mass density $\rho = 2100 \frac{\text{kg}}{\text{m}^3}$, and Young's modulus $E = 0.255 \times 105$ MPa [10]. Based on these physical parameters, the dimensionless coefficients of Equations (2) and (3) are given as follows: $= 0.01, \omega = 3.06309, \alpha = 14.4108, \beta = 0.05, \gamma = 3.2746, \lambda = 0.89663, f = 0.01, \Omega = \omega + \sigma$, and $\sigma = 0.0$. In addition, the controller parameters are selected

to be $\delta_1 = \delta_2 = 2$, $\eta = 1$, and $\tau_1 = \tau_2 = 0.0$ unless otherwise is mentioned. The nonlinear dynamics of the considered self-excited have been explored with the aid of Equations (2), (3), (24), (25), (28), and (30) in this section, where Section 3.1 is assigned to investigate the nonlinear oscillations of the uncontrolled self-excited system, and Section 3.2 is dedicated to studying the effects of the IRC parameters (δ_1 , δ_2 , and η) when the loop delays. In addition, the influence of the time delays on the control performance has been discussed in Section 3.3.

3.1. Uncontrolled Self-Excited System ($\delta_1 = \delta_2 = 0$)

The dynamical characteristics of the considered self-excited system have been explored within this section before control (i.e., when $\delta_1 = \delta_2 = 0.0$). It is worth remembering from Equation (20) that the parameter σ describes the closeness of the excitation frequency Ω to the system natural frequency ω , where $\Omega - \omega = \sigma$. Accordingly, the parameter σ is used in the whole article to describe the closeness of the excitation frequency Ω to the system natural frequency ω , where ω is constant (i.e., $\omega = 3.06309$). Figure 3a shows the cantilever beam system oscillation amplitude against σ when $f = 0.01$. It is clear from the figure that the uncontrolled self-excited system can oscillate by one of the four oscillation modes depending on the excitation frequency, which are mono-stable periodic motion (when $-0.094 < \sigma < 0.11$), bi-stable periodic motion (when $-0.11 < \sigma < 0.094$), unstable periodic motion (when $-0.145 > \sigma$ and $\sigma > 0.11$), and simultaneous stable and unstable periodic motion (when $-0.145 < \sigma < -0.11$). It is worth mentioning that Figure 3a has been obtained via solving Equation (28) numerically using σ as main the bifurcation parameter along the interval $-0.5 \leq \sigma \leq 0.5$ [39]. In addition, the obtained solution stability has been investigated at the same time via checking the eigenvalues of Equation (30).

Accordingly, to investigate the nature of the unstable motion reported in Figure 3a, the system bifurcation diagram has been established in Figure 3b via solving Equation (2) (when $\delta_1 = 0$) numerically using MATLAB ODE45 solver. Using σ as a bifurcation parameter with step-size $\Delta\sigma = 0.0025$, Equation (2) has been solved numerically along the time interval $0 \leq t \leq 6000$, and the Poincaré map of the steady-state temporal oscillation (i.e., $x(t)$ on the time interval $5000 \leq t \leq 6000$) has been plotted against σ . It is clear from Figure 3b that the unstable periodic motion that occurs on the intervals $\sigma < -0.11$ and $\sigma > 0.11$ is a bounded motion, which implies that the considered self-excited system may perform either quasi-periodic or chaotic motion when $-0.11 > \sigma$ and $\sigma > 0.11$. Therefore, To distinguish the nature of this aperiodic bounded oscillation if it is either quasi-periodic or chaotic on the intervals $\sigma < -0.11$ and $\sigma > 0.11$, the steady-state temporal oscillations (i.e., $x(t)$ on the time interval $5000 \leq t \leq 6000$) that used to obtain Figure 3b is fed to the 0–1 chaotic test algorithm to obtain Figure 3c. It is clear from Figure 3c that the output of the 0–1 chaotic test algorithm is lower than 0.1, which confirms that the system performs only quasi-periodic oscillation on the intervals $\sigma < -0.11$ and $\sigma > 0.11$ [40]. Based on Figure 3b,c, we can confirm that the self-excited system can perform only two types of bounded motion that are periodic oscillation (corresponding to the solid line in Figure 3a) and quasi-periodic oscillation (corresponding to the dotted line in Figure 3a).

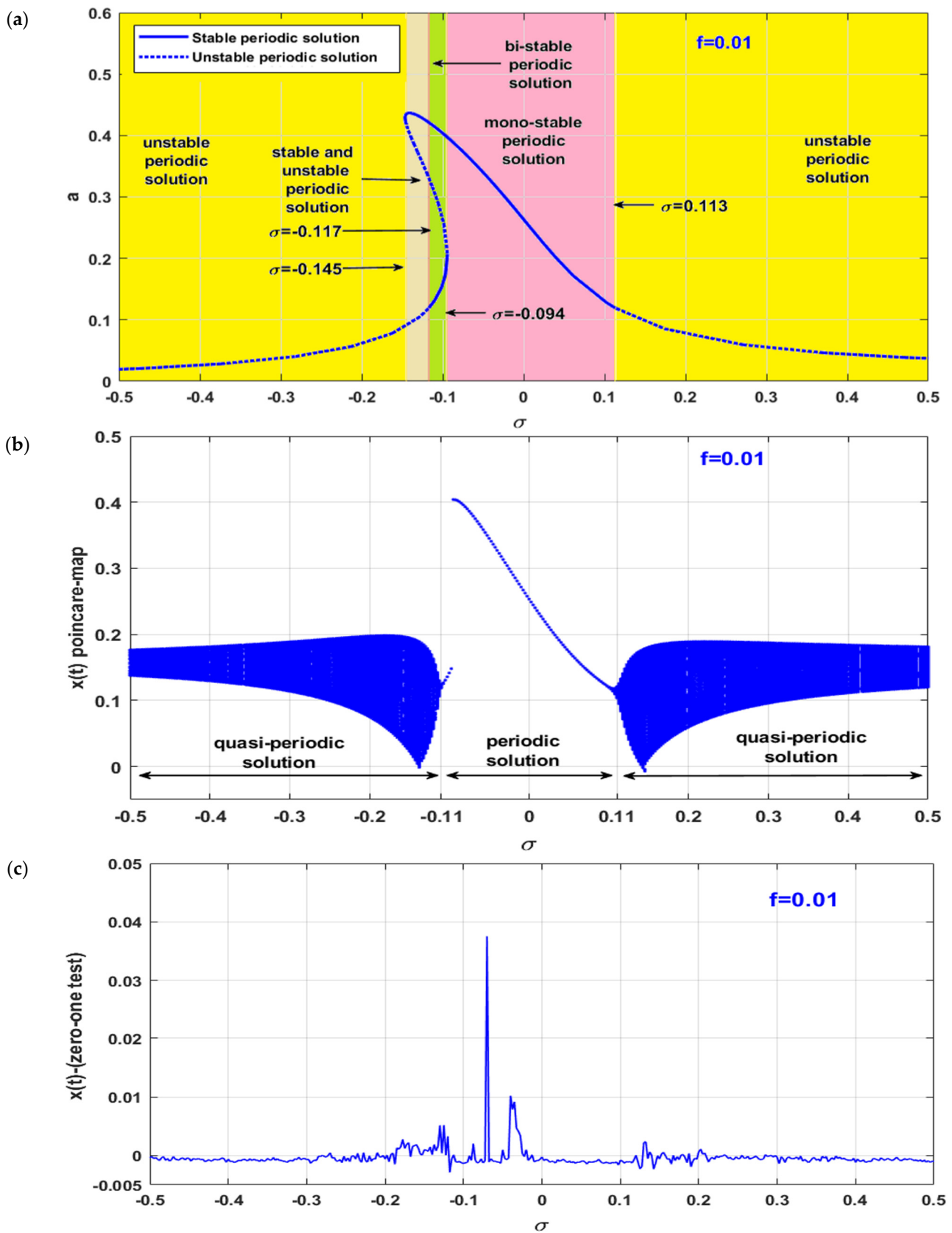


Figure 3. (a) The self-excited system frequency-response curve when the excitation force amplitude $f = 0.01$, (b) the corresponding bifurcation diagram, and (c) the corresponding zero-one chaotic test.

The steady-state temporal oscillation of the uncontrolled self-excited system is numerically simulated as shown in Figures 4–6 via solving Equation (2) (when $\delta_1 = 0$) using MATLAB ODE45 at three different values of the excitation frequency $\Omega = \omega + \sigma$ that have been selected according to Figure 3, where Figure 3a shows that the considered system has two stable vibration amplitudes $a \cong 0.15$ and $a \cong 0.4$ when $\sigma = -0.1$. Accordingly, Equation (2) has been solved numerically when $\Omega = \omega - 0.1$ at the two initial conditions $x(0) = \dot{x}(0) = 0.5$ and $x(0) = 0.15, \dot{x}(0) = 0$ to capture the two periodic solutions that are expected based on Figure 3a when $\sigma = -0.1$, where the simulation results have been illustrated in Figure 4. It is clear from Figure 4 that the self-excited system can respond with one of two periodic motions depending on the initial condition. Comparing Figure 4 with Figure 3a at $\sigma = -0.1$, one can confirm the excellent correspondence between the analytical and numerical results. Figure 5 shows the self-excited system steady-state temporal oscillation, phase trajectory, Poincaré map, and frequency spectrum according to Figure 3a when $\sigma = 0.0$ (i.e., when $\Omega = \omega$). The figure demonstrates that the uncontrolled system has only one periodic solution (with oscillation amplitude $a \cong 0.25$) regardless of the initial conditions. Comparing Figure 5 with Figure 3a at $\sigma = 0.0$, we can see the excellent congruence between the analytical and numerical results. Numerical simulation for the steady-state temporal oscillation, phase trajectory, Poincaré map, and frequency spectrum of the uncontrolled system has been illustrated in Figure 6 according to Figure 3a at $\sigma = 0.2$. It is clear from the Poincaré map shown in Figure 6b that the uncontrolled system exhibits quasi-periodic oscillation (i.e., unstable periodic motion) at $\Omega = \omega + 0.2$, which agrees with high accuracy to the analytical solution shown in Figure 3a.

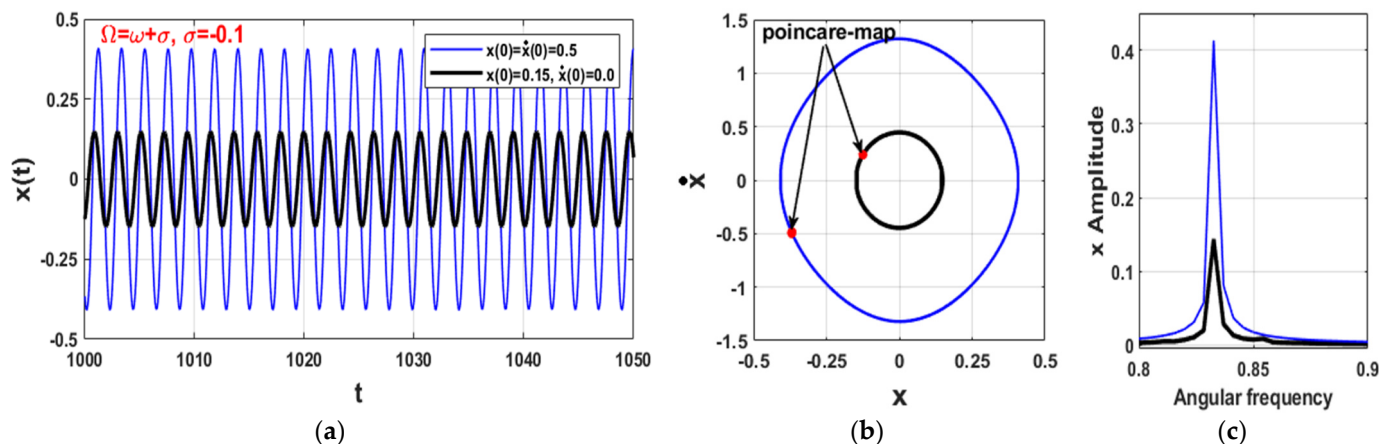


Figure 4. Self-excited system instantaneous vibrations according to Figure 3a when $\sigma = -0.1$ at the initial conditions $x(0) = \dot{x}(0) = 0.5$ and $x(0) = 0.15, \dot{x}(0) = 0.0$: (a) time history, (b) phase trajectory and the corresponding Poincaré map, and (c) frequency spectrum.

Oscillation amplitude of the uncontrolled self-excited system is plotted versus the detuning parameter σ at various levels of the excitation force amplitude (i.e., when $f = 0.001, 0.005, 0.01, \text{ and } 0.02$) as shown in Figure 7a via solving Equation (28) using σ as the bifurcation control parameter, where the solution stability is explored via investigating the eigenvalues of the linear dynamical system given by Equation (30). The figure illustrates that the self-excited system may lose its periodic motion either via saddle-node or Hopf bifurcation. Furthermore, even though increasing the excitation force increases the system oscillation amplitude, it stabilizes the system motion over a wide range of excitation frequencies on both the left and right sides of $\sigma = 0.0$. Therefore, to explore bifurcation behaviors, the oscillation amplitude at a wide range of the excitation force, Equation (28) has been solved as an implicit equation of a and f at different values of σ as shown in Figure 7b. It is clear from Figure 7b that the considered system may lose its stability at the low levels of the excitation force to oscillate with quasi-periodic motion. To visualize the system vibration amplitude in $f - \sigma$ plane, Equation (28) has been solved as an implicit

equation of the three variables (a, f, σ) as shown in Figure 8a, and the corresponding stability chart is illustrated $f - \sigma$ plane as shown in Figure 8b. It is clear from Figure 8b that the increase in the excitation force amplitude stabilizes the system oscillations at a wide band of the excitation.

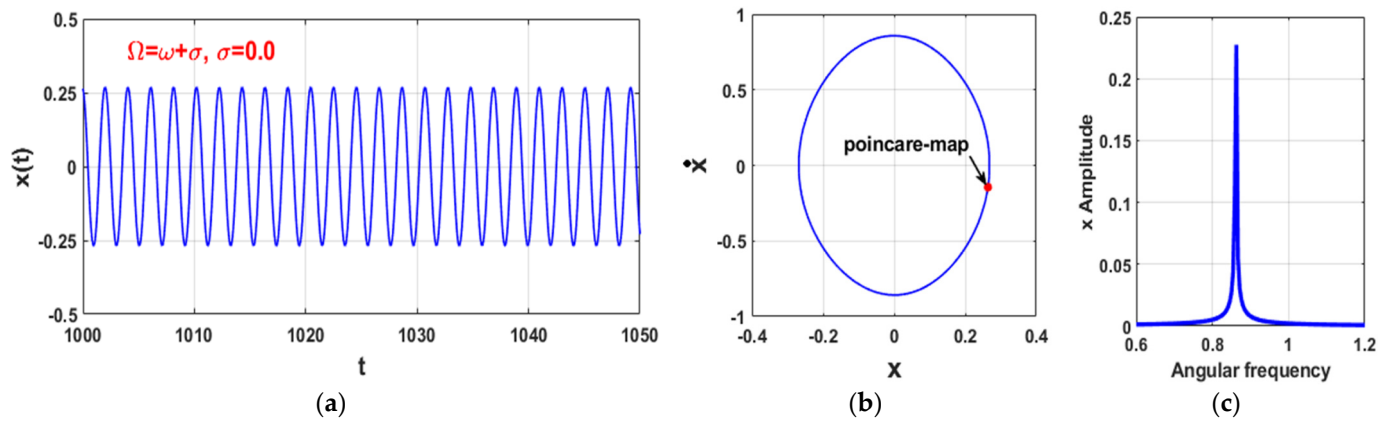


Figure 5. Self-excited system instantaneous vibrations according to Figure 3a when $\sigma = 0.0$: (a) time history, (b) phase trajectory and the corresponding Poincaré map, and (c) frequency spectrum.

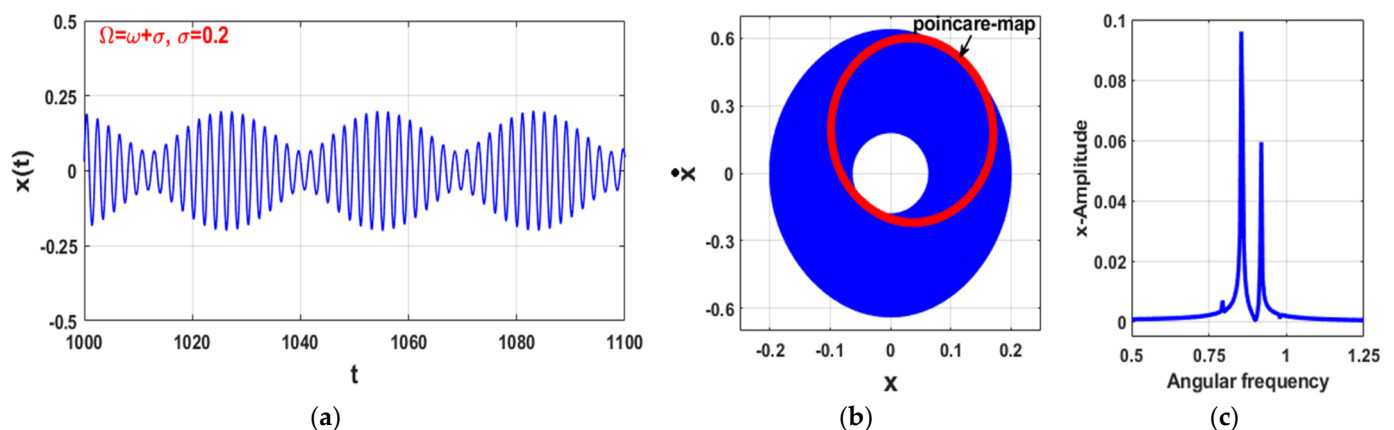


Figure 6. Self-excited system instantaneous vibrations according to Figure 3a when $\sigma = 0.2$: (a) time history, (b) phase trajectory and the corresponding Poincaré map, and (c) frequency spectrum.

To confirm the accuracy of the stability chart given in Figure 8b, Equation (2) (when $\delta_1 = 0$) has been solved numerically using Matlab solver ODE45 according to the marked points P_1 and P_2 that shown in Figure 8b, where the numerical results are shown in Figures 9 and 10, respectively. Figure 9 shows the temporal oscillation, phase trajectory, Poincaré map, and frequency spectrum of the uncontrolled system according to the point P_1 (i.e., when $f = 0.04$, $\sigma = 0.4$) shown in Figure 8b. It is clear from Figure 9 that the system performs stable periodic motion as expected from Figure 8b. In addition, Figure 10 illustrates the temporal oscillation, phase trajectory, Poincaré map, and frequency spectrum of the uncontrolled system according to the point P_2 (i.e., when $f = 0.02$, $\sigma = 0.4$) shown in Figure 8b. It is clear from Figure 10 that the system exhibits quasi-periodic oscillation (i.e., unstable periodic motion).

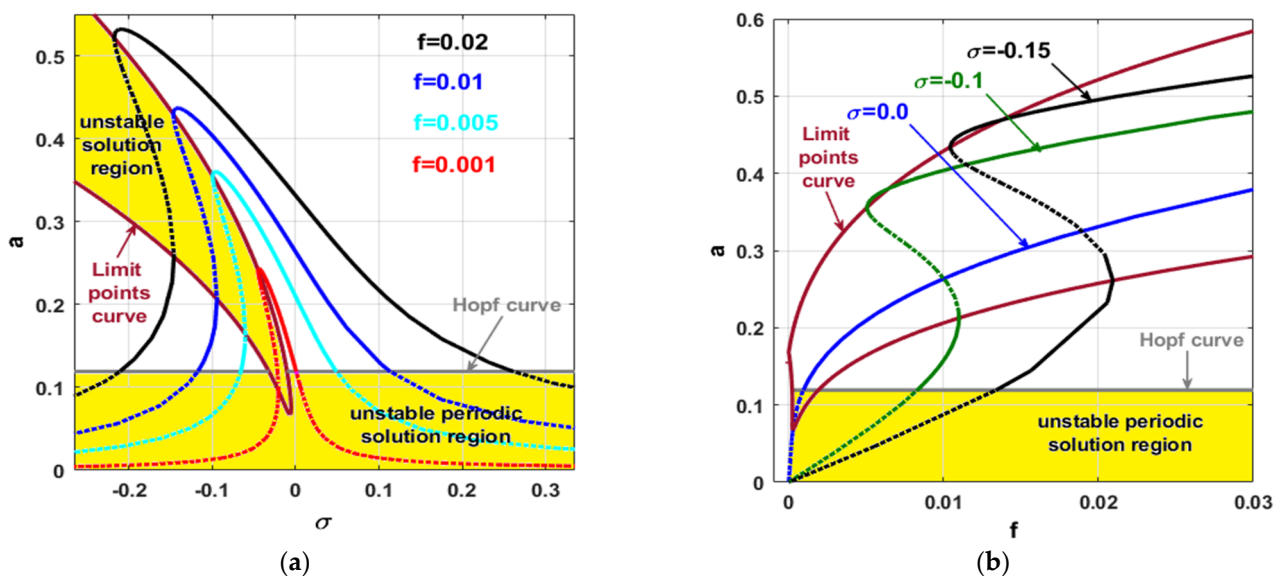


Figure 7. (a) Self-excited system steady-state vibration amplitude versus the excitation frequency at four different values of the excitation force, and (b) Self-excited system steady-state vibration amplitude versus the excitation force at different values of σ .

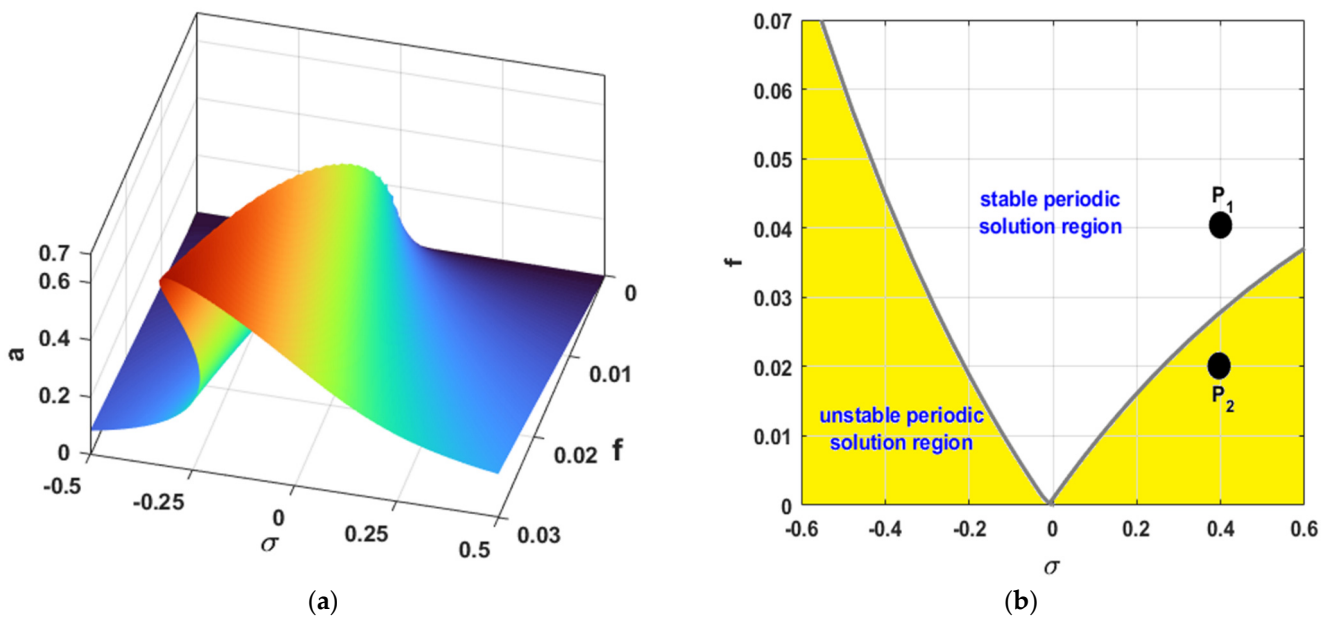


Figure 8. (a) Three-dimensional visualization for the steady-state vibration amplitude in $f - \sigma$ plane, and (b) the corresponding stability chart in $f - \sigma$ plane.

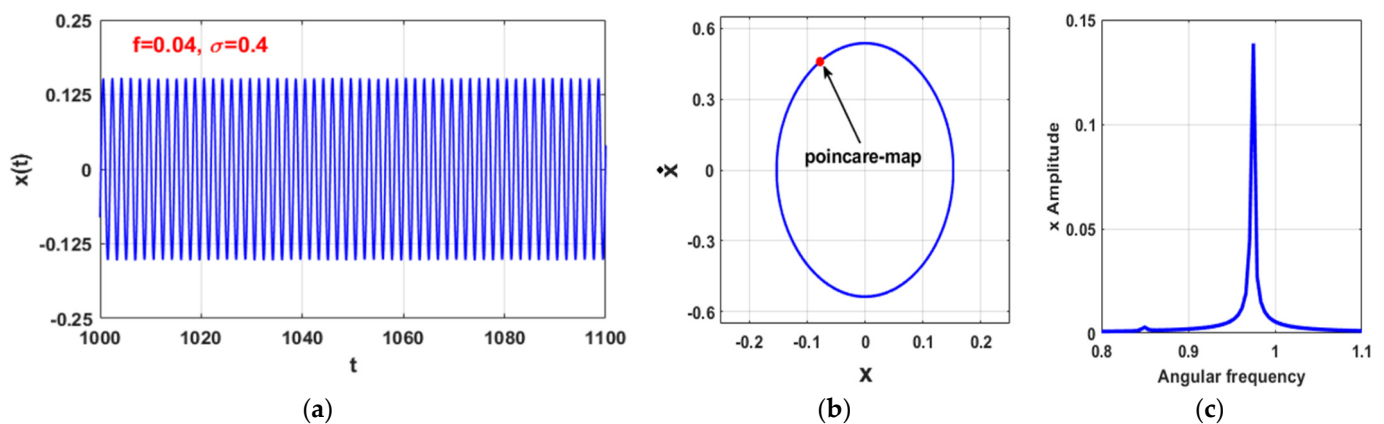


Figure 9. Self-excited system instantaneous vibrations according to the point P_1 that marked on Figure 8b (i.e., when $f = 0.04$, $\sigma = 0.4$): (a) time history, (b) phase trajectory and the corresponding Poincaré map, and (c) frequency spectrum.

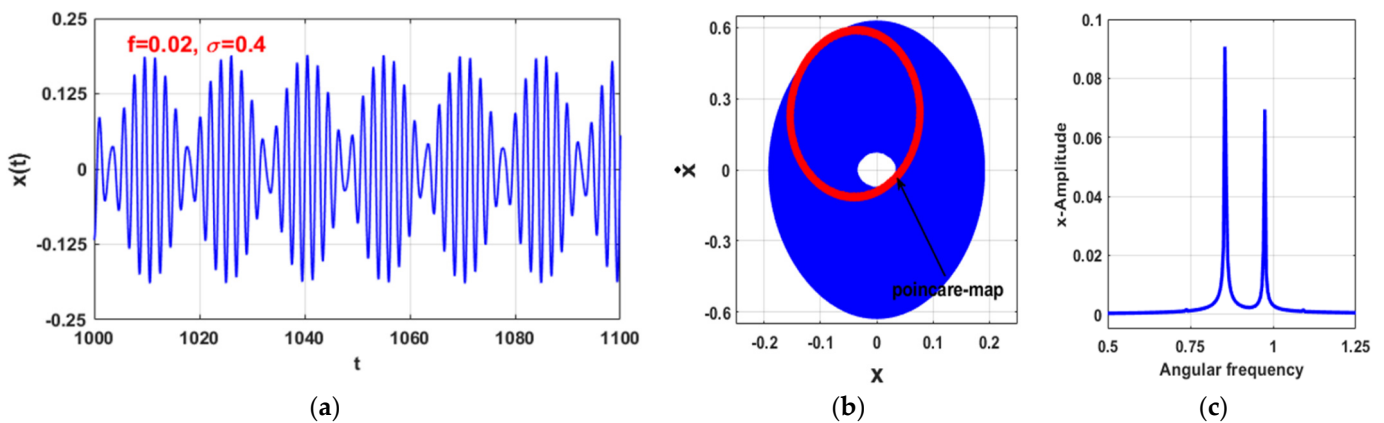


Figure 10. Self-excited system instantaneous vibrations according to the point P_2 that marked on Figure 8b (i.e., when $f = 0.02$, $\sigma = 0.4$): (a) time history, (b) phase trajectory and the corresponding Poincaré map, and (c) frequency spectrum.

3.2. The Controlled Self-Excited System with Zero Time Delays ($\tau_1 = \tau_2 = 0$)

The performance of the proposed control strategy in stabilizing the unstable motion and eliminating the transversal oscillation of the studied self-excited system has been discussed within this section, considering the loop delays are zeros (i.e., when $\tau_1 = \tau_2 = 0$). Before proceeding further, let us first examine the derived slow-flow modulating equations given by Equations (24) and (25). It is clear from Equation (24) that the coupling of the proposed integral resonant controller to the studied system has modified its negative damping coefficient ($-\mu$) to the equivalent control damping μ_c that can be expressed as follows (when $\tau_1 = \tau_2 = 0$):

$$\mu_c = -\mu + \frac{\delta_1 \delta_2}{(\eta^2 + \omega^2)} \quad (31)$$

Based on Equation (31), one can simply deduce that the control damping (μ_c) of the controlled self-excited system is proportional to the product of δ_1 and δ_2 (i.e., $\mu_c \propto \delta_1 \delta_2$), and inversely proportional η^2 ($\mu_c \propto \frac{1}{\eta^2}$). Accordingly, one can expect that the selection of the controller gains (δ_1 , δ_2 , and η) in such a way that maximizes the expression $\frac{\delta_1 \delta_2}{\eta^2}$ will improve the controller efficiency in both mitigating the nonlinear oscillations and stabilizing the unstable motion of the considered self-excited system. Based on Equation (31), the equivalent damping coefficient (μ_c) is plotted as a function of the two variables δ_1 and δ_2 when $\mu = 0.01$, $\omega = 3.06309$, and $\eta = 1$ as shown in Figure 11. It is clear from the figure that

the controlled self-excited system damping coefficient is a monotonic increasing function of the product of both δ_1 and δ_2 either when $\delta_1 > 0$ & $\delta_2 > 0$ (as shown in Figure 11a) or when $\delta_1 < 0$ & $\delta_2 < 0$ (as shown in Figure 11b).

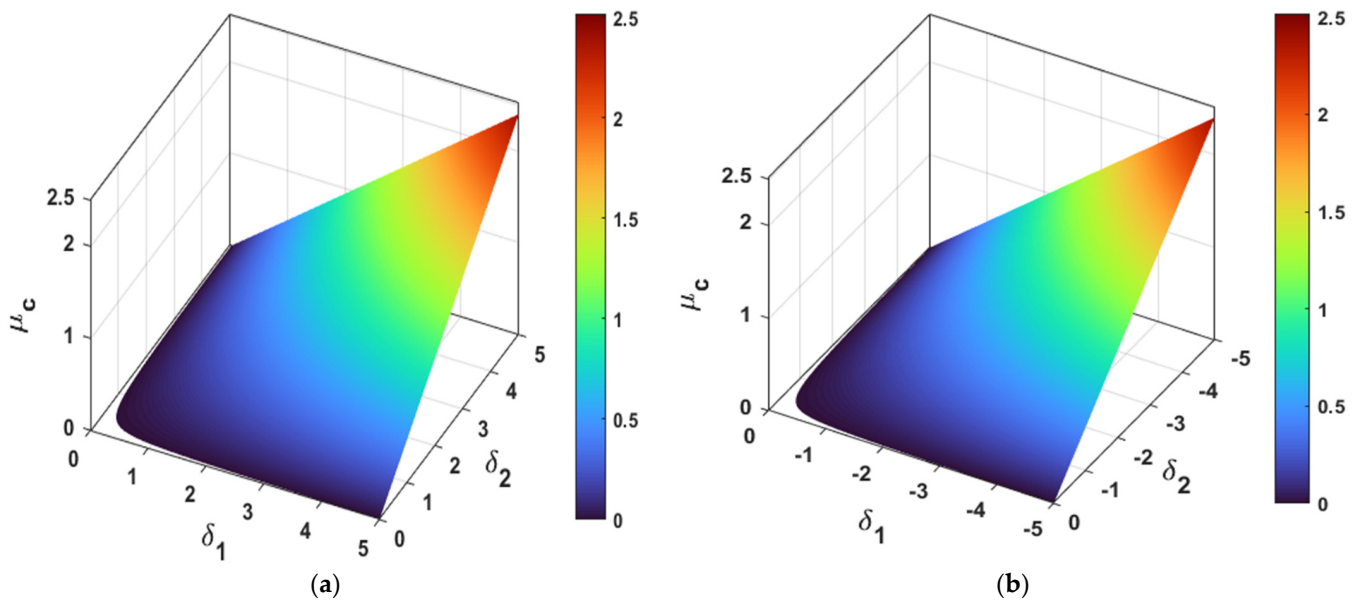


Figure 11. The equivalent control damping coefficient μ_c of the self-excited system as a function of both the two variables δ_1 and δ_2 : (a) μ_c when $\delta_1 \geq 0$ and $\delta_2 \geq 0$, and (b) μ_c when $\delta_1 \leq 0$ and $\delta_2 \leq 0$.

Based on Equation (31) and Figure 11, the vibration amplitude (a) of the self-excited system is obtained via solving Equation (28) as a function of the two variables δ_1 and δ_2 as shown in Figure 12, where Figure 12a illustrates the system oscillation amplitude in $\delta_1 - \delta_2$ plane when $\delta_1 \geq 0$ & $\delta_2 \geq 0$, and Figure 12b shows the system oscillation amplitude in $\delta_1 - \delta_2$ plane when $\delta_1 \leq 0$ & $\delta_2 \leq 0$. Comparing Figure 12a,b, one can find that the two figures are identical, where the vibration amplitude is a monotonic decreasing function of the product of δ_1 and δ_2 provided that $\delta_1 \times \delta_2 > 0$ (i.e., $\delta_1 \leq 0$ & $\delta_2 \leq 0$ or $\delta_1 \geq 0$ & $\delta_2 \geq 0$). It is clear from Figures 11 and 12 that the increase in the quantity $(\delta_1\delta_2)$ via increasing δ_1 or δ_2 or both is resulting in the increase in the system damping coefficient (as in Figure 11), which in turn decreases the steady-state oscillation amplitude of the targeted system (as in Figure 12).

To explore the efficiency of the applied IRC in mitigating the nonlinear oscillation of the considered system on a wide range of the excitation frequency Ω ($\Omega = \omega + \sigma$), Equation (28) has been solved as an implicit equation of the three variables a , σ , and $\delta_1\delta_2$ as shown in Figure 13a, where $\delta_1\delta_2$ has been treated as one variable. By examining Figure 13a, one can see that the controlled self-excited system may respond as a linear system with very small oscillation amplitude regardless of the excitation frequency when the product of the control and feedback gains exceed a specific limit. To visualize the obtained results in more clear form, Equation (28) has been solved again as an implicit equation of the two variables a and σ at three fixed values of $\delta_1\delta_2$ as shown in Figure 13b. It is clear from the figure that the increase in $\delta_1\delta_2$ decreases the system oscillation amplitude and eliminates the motion bifurcation. In addition, Figure 13b confirms that the unstable periodic solution (i.e., quasi-periodic) of the uncontrolled self-excited system that reported in Figure 3 when $\sigma < -0.11$ and $\sigma > 0.11$, has been stabilized as shown in Figure 13b.

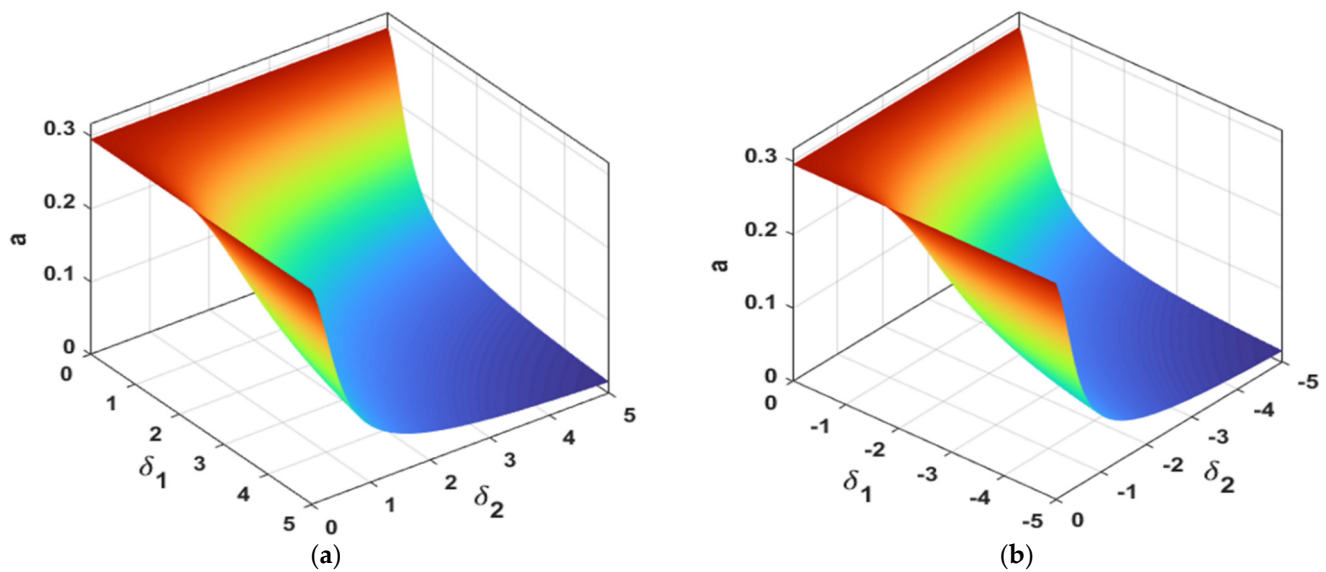


Figure 12. The steady-state oscillation amplitude (a) of the self-excited system as a function of both the two variables δ_1 and δ_2 : (a) oscillation amplitude when $\delta_1 \geq 0$ and $\delta_2 \geq 0$, and (b) oscillation amplitude when $\delta_1 \leq 0$ and $\delta_2 \leq 0$.

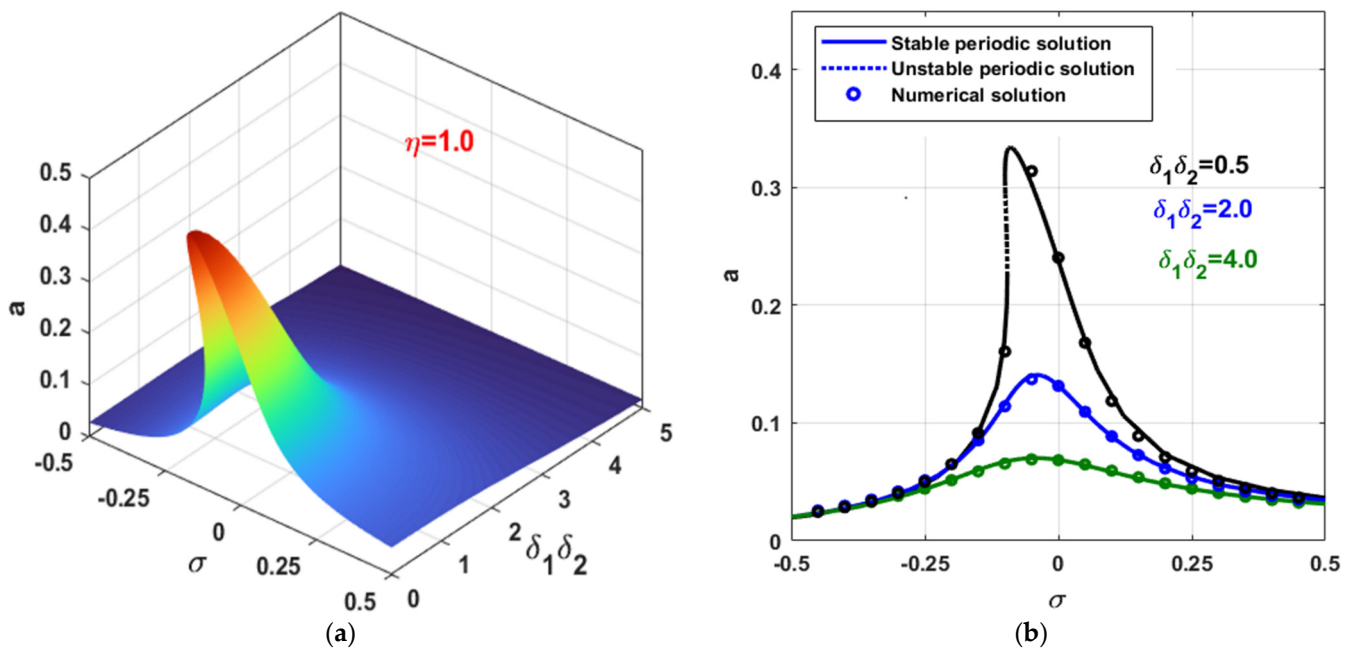


Figure 13. (a) Three-dimensional visualization of the self-excited system vibration amplitude as a function of the two variables $\delta_1\delta_2$ and σ , and (b) self-excited system frequency response at three different values of $\delta_1\delta_2$.

It is worth mentioning that the obtained frequency-response equation (Equation (28)) governs the system oscillation amplitude as a function of the system and controller parameters, where this equation has been derived based on an approximate solution (i.e., based on Equations (4)–(7)). Therefore, to validate the accuracy of the derived frequency-response equation, the numerical solution of the controlled system original equations (i.e., Equations (2) and (3)) has been obtained and compared with the analytical solution given by Equation (28), as shown in Figure 13b, where the small circles represent the numerical solution. The procedure of obtaining the numerical solution is as follows:

1. Let the bifurcation parameter is σ with the initial value $\sigma_I = -0.5$, final value $\sigma_F = 0.5$, and step-size $\Delta\sigma = 0.05$;
2. Set $\sigma = \sigma_I$, and $\Omega = \omega + \sigma$;
3. Solve the system temporal Equations (2) and (3) numerically using ODE45 MATLAB solver on the time interval $0 \leq t \leq 6000$ to get the steady-state oscillation;
4. Find the maximum value of $x(t)$ on the time interval $5900 \leq t \leq 6000$ as x_{max} ;
5. Set $a = x_{max}$;
6. Increase σ by $\Delta\sigma$, and go to step (2).

According to the above algorithm, the steady-state oscillation amplitude has been obtained numerically using σ as the bifurcation parameter, where the numerical solution of the steady-state amplitude has been plotted against the solution obtained using Equation (28) when $\delta_1\delta_2 = 0.5, 2.0$, and 4.0 as shown in Figure 13b. It is clear from the figure the excellent correspondence between the analytical and numerical results.

In addition, to investigate transient behaviors of the controlled system when increasing $\delta_1\delta_2$ online, the time-response and phase trajectory of both the system and controller have been simulated according to Figure 13b at $\sigma = 0$ as shown in Figure 14 when increasing $\delta_1\delta_2$ from 0.5 to 2.0 at the time instance $t = 150$, and then increasing $\delta_1\delta_2$ from 2.0 to 4.0 at $t = 200$. It is clear from the figure that the system oscillation amplitude is a monotonic decreasing function of the product of the control and feedback signals gains. Moreover, no overshoot has been noticed for both the system and the controller during the increase $\delta_1\delta_2$ from 0.5 to 2.0 , and then from 2.0 to 4.0 , which demonstrate the feasibility of the proposed control strategy in both vibration suppression and stabilizing the unstable motion of such systems.

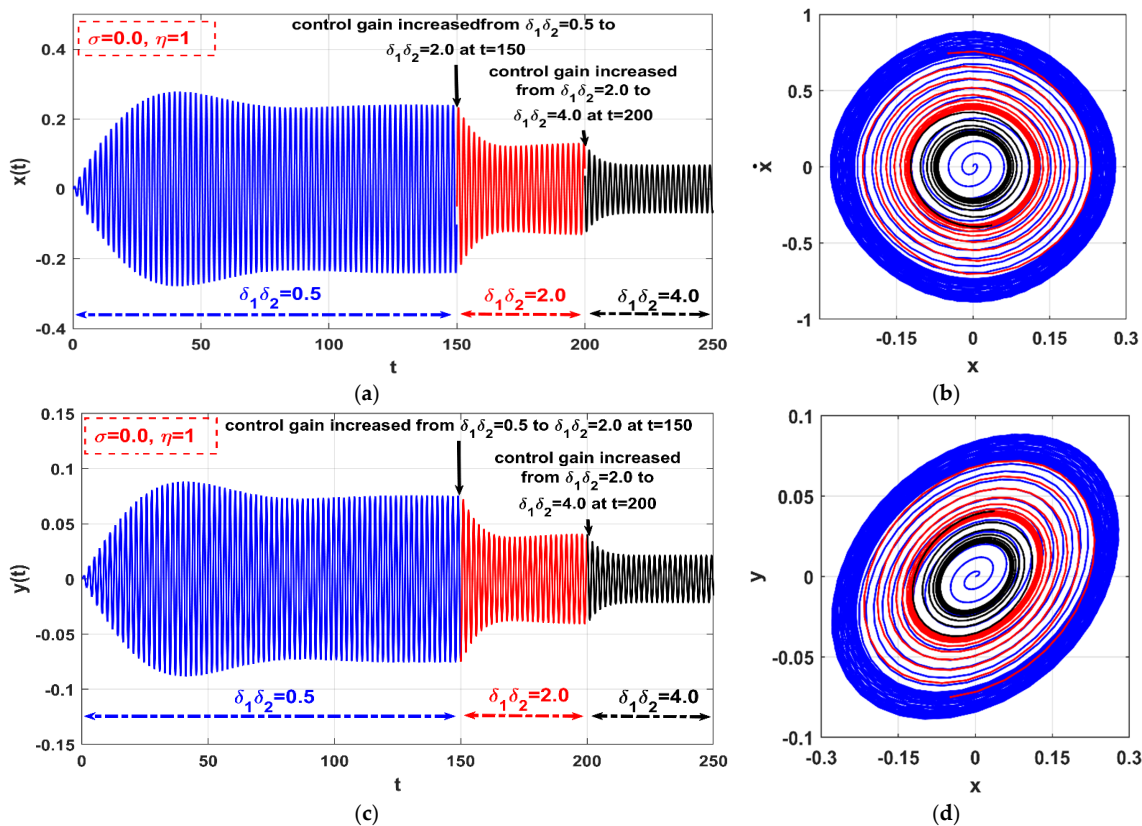


Figure 14. The temporal oscillations and the phase trajectories of both the self-excited system and the integral resonant controller according to Figure 13 at $\sigma = 0$ when increasing $\delta_1\delta_2$ online from 0.5 to 2 at $t = 150$, and then from 2 to 4 at $t = 200$: (a) temporal oscillations of the self-excited system, (b) phase trajectory of the self-excited system, (c) temporal oscillations of the controller, and (d) orbit-plot of the system and controller.

The influence of the internal feedback gain η on the controller efficiency has been illustrated in Figure 15a, where the frequency-response equation (Equation (28)) has been solved as an implicit function of a , σ , and η at $\delta_1\delta_2 = 2.0$. It is clear from the figure that the self-excited system oscillation amplitude is a monotonic increasing function of η on the excitation frequency interval $\Omega = \omega + \sigma$, $\sigma = [-0.5, 0.5]$. To validate the accuracy of Figure 15a, Equation (28)) has been solved again as an implicit function of the two variables a and σ at various values of η (i.e., at $\eta = 1.0, 3.0$, and 5.0) when fixing $\delta_1\delta_2 = 2.0$ as shown in Figure 15b. Moreover, the numerical solution of the steady-state oscillation amplitude has been compared with the obtained analytical results. In general, Figure 15 demonstrates that the increase in the internal feedback gain (η) may degrade the controller efficiency in suppressing the self-excited system oscillation hat is agrees with the definition given by Equation (31) (i.e., $\mu_c = -\mu + \frac{\delta_1\delta_2}{\omega^2 + \eta^2}$), where the increase in η decreases the equivalent damping coefficient, which in turn increases the system oscillation amplitude.

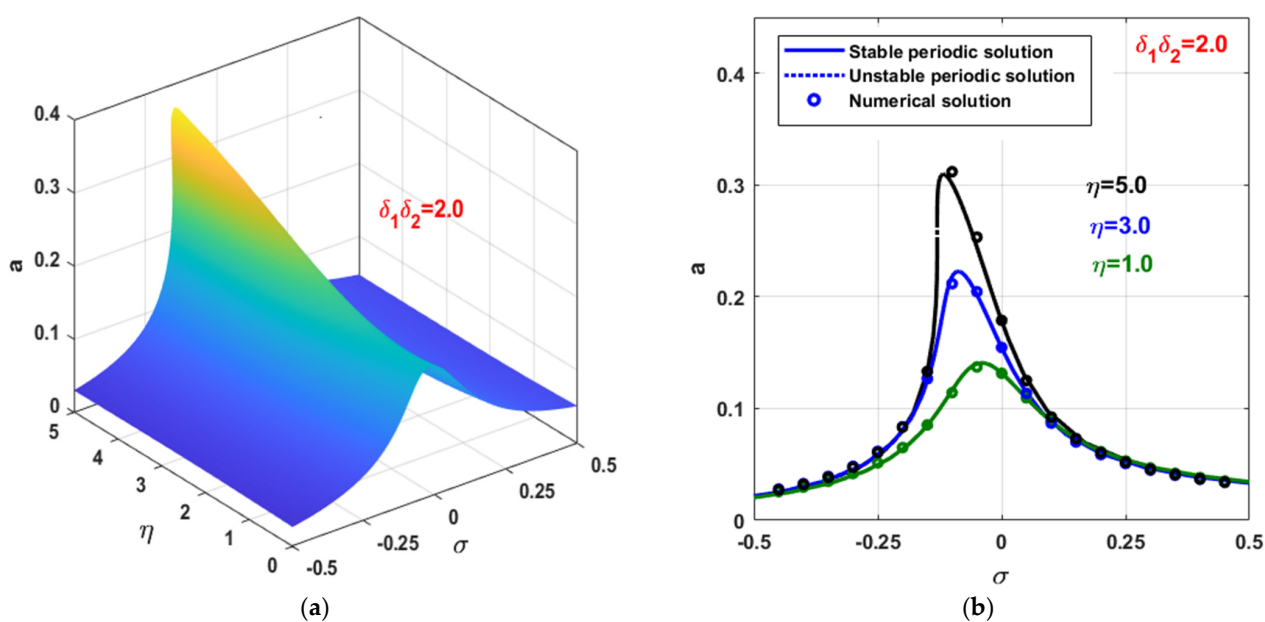


Figure 15. (a) Three-dimensional visualization of the self-excited system vibration amplitude as a function of the two variables η and σ when $\delta_1\delta_2 = 2.0$, and (b) self-excited system frequency-response curve at three different values of the controller internal feedback gain η (i.e., $\eta = 1.0, 3.0$, and 5.0) when $\delta_1\delta_2 = 2.0$.

To investigate the robustness of the applied control method against the system instability at a wide range of the external excitations force f , Equation (28) has been solved as an implicit function of the three variables a , σ , and f when $\delta_1\delta_2 = 4.0$ and $\eta = 1$, as shown in Figure 16a. It is clear from the figure that the oscillation amplitude is a monotonic increasing function of f . However, the self-excited system exhibits a mono-stable periodic solution along the excitation frequency interval $-0.5 \leq \sigma \leq 0.5$, even if the excitation force becomes 10 times the excitation amplitude used to obtain Figure 3a (i.e., even if $f = 0.1$). To validate Figure 16a numerically, Equation (28) has been solved as an implicit function of the two variables a and σ at $f = 0.01, 0.05$, and 0.1 when $\delta_1\delta_2 = 4.0$ and $\eta = 1$, as shown in Figure 16b, where the numerical solution of the steady-state oscillation amplitude has been compared with the obtained analytical solution as small circles. Moreover, to visualize the steady-state and the transient oscillations of the controlled self-excited system when increasing the excitation force amplitude f online, the time-response and the corresponding phase trajectory of both the considered system and the IRC has been illustrated according to Figure 16b at $\sigma = 0$ (i.e., when $\sigma = 0, \delta_1\delta_2 = 4.0, \eta = 1$) in Figure 17 when increasing the excitation force f from 0.01 to 0.05 at the time instant $t = 50$, and then increasing f

from 0.05 to 0.1 at $t = 100$. It is clear from Figure 17 that the controlled system oscillation amplitude is a monotonic increasing function of f ; however, no overshoot for the system oscillation amplitude has been shown when the excitation force has abruptly increased either from 0.01 to 0.05 or from 0.05 to 0.1.

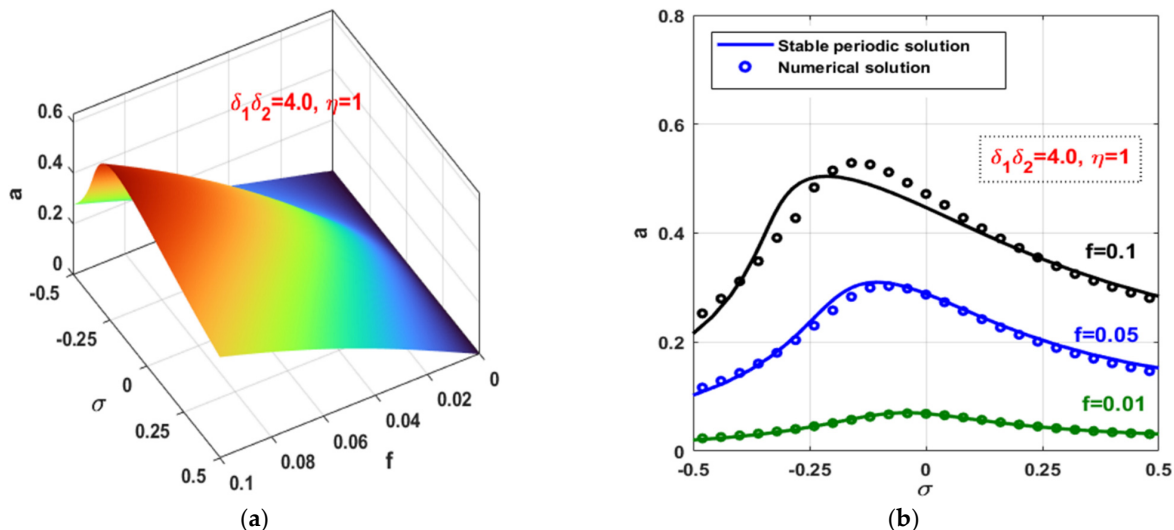


Figure 16. (a) Three-dimensional visualization of the self-excited system vibration amplitude as a function of the two variables f and σ , when $\delta_1\delta_2 = 4.0$, $\eta = 1.0$, and (b) self-excited system frequency-response curve at three different values of the excitation force amplitude f (i.e., $f = 0.01$, 0.05 , and 0.1) when $\delta_1\delta_2 = 4.0$, $\eta = 1.0$.

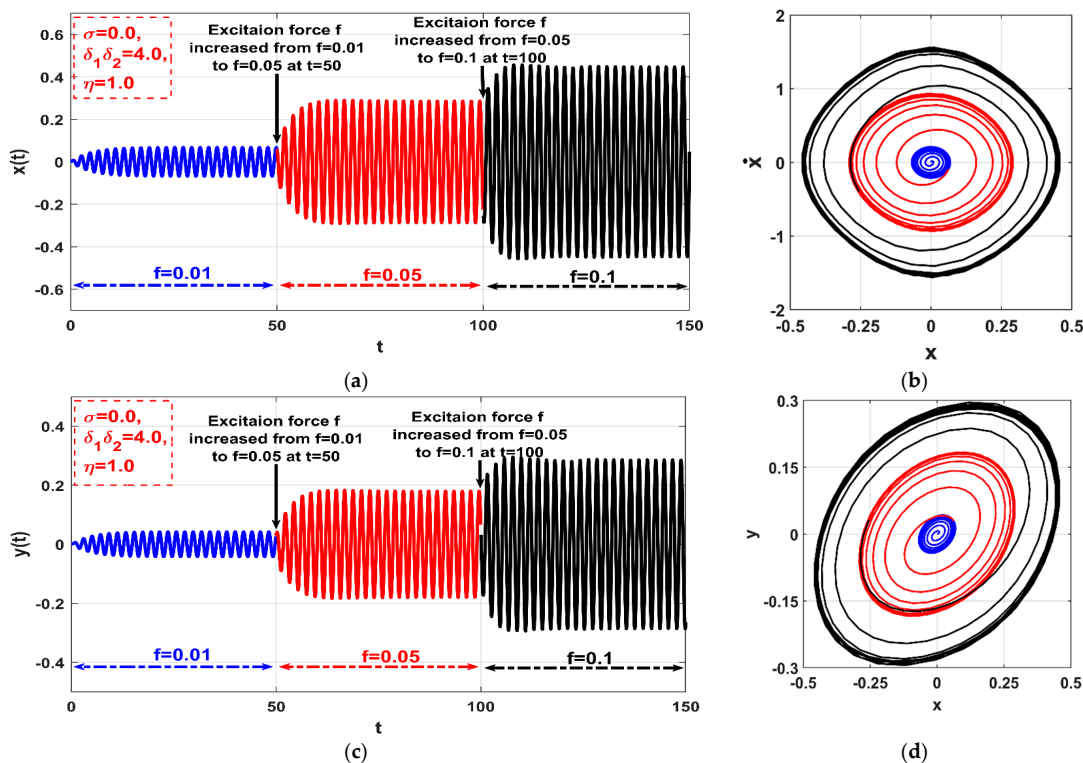


Figure 17. The temporal oscillations and phase trajectories of both the self-excited system and the integral resonant controller according to Figure 13 at $\sigma = 0$ when increasing $\delta_1\delta_2$ online from 0.5 to 2 at $t = 150$, and then from 2 to 4 at $t = 200$: (a) temporal oscillations of the self-excited system, (b) phase trajectory of the self-excited system, (c) temporal oscillations of the controller, and (d) orbit-plot of the system and controller.

3.3. The Controlled Self-Excited System with Time Delays

The influences of the loop delays (τ_1 and τ_2) on both the controller efficiency and system stability has been discussed within this section. Based on the derived slow-flow modulating equations given by Equations (24) and (25), one can simply deduce that the damping coefficient of the controlled self-excited system ($\mu_{c\tau}$) may be expressed as follows:

$$\mu_{c\tau} = -\mu + \frac{\delta_1\delta_2}{(\eta^2 + \omega^2)} \cos(\omega\tau_1 + \omega\tau_2) + \frac{\eta\delta_1\delta_2}{\omega(\eta^2 + \omega^2)} \sin(\omega\tau_1 + \omega\tau_2) \quad (32)$$

As Equation (32) implies, the equivalent damping coefficient of the time-delayed system is a periodic function of the total time delays of the control loop (i.e., $\tau_1 + \tau_2$). Accordingly, $\mu_{c\tau}$ has been plotted as a function of the two variables $\tau_1 + \tau_2$ and $\delta_1\delta_2$ as shown in Figure 18a. By examining Figure 18a, we can notice that $\mu_{c\tau}$ is a periodic function of $\tau_1 + \tau_2$, where the oscillation amplitude of this function is a monotonic increasing function of $\delta_1\delta_2$. Therefore, if we fix $\delta_1\delta_2$ constant (say $\delta_1\delta_2 = 5.0$) and try to examine $\mu_{c\tau}$ along $\tau_1 + \tau_2$ axis, we can find that the controlled self-excited system may have a positive damping coefficient on some intervals of the loop delays and a negative damping coefficient on other intervals. Accordingly, Equation (28) has been solved as an implicit equation of the three variables a , $\delta_1\delta_2$, and $\tau_1 + \tau_2$, as shown in Figure 18b when $\sigma = 0.0$. Comparing Figure 18a with Figure 18b, one can find that the system oscillation amplitude in Figure 18b is a monotonic decreasing function of $\delta_1\delta_2$ at the time-delay intervals at which $\mu_{c\tau} > 0$ as shown in Figure 18a. However, the system oscillation amplitude in Figure 18b is a monotonic increasing function of $\delta_1\delta_2$ at the time-delay intervals at which $\mu_{c\tau} < 0$ as depicted in Figure 18a.

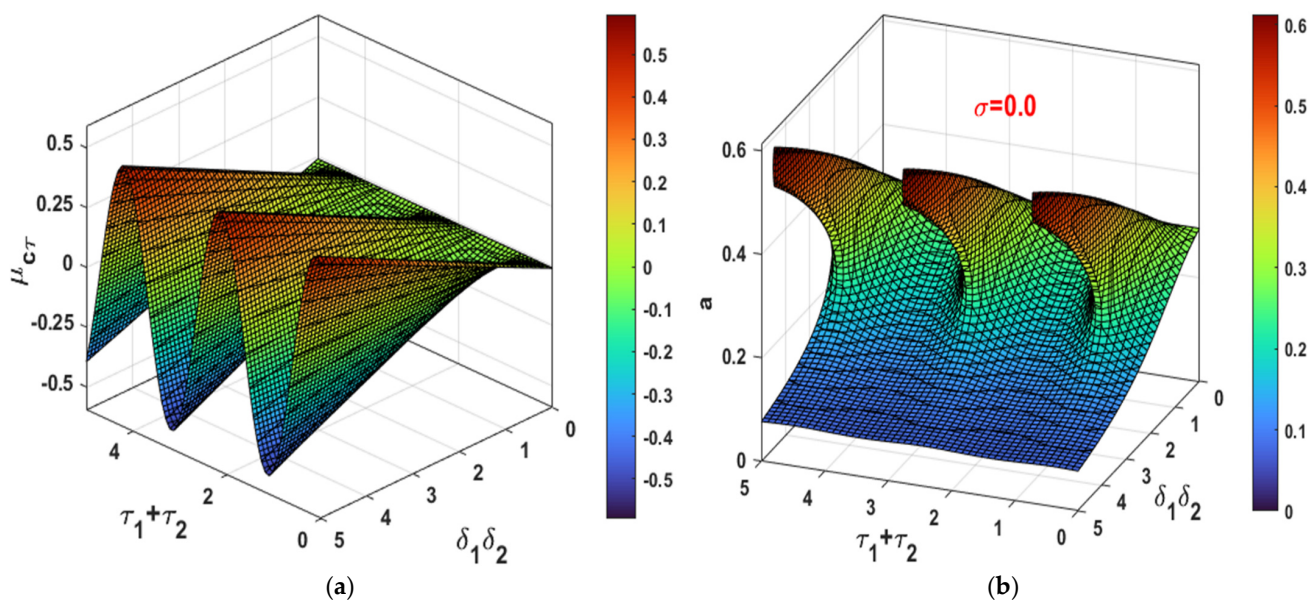


Figure 18. (a) The time-delayed equivalent damping coefficient $\mu_{c\tau}$ as a function of the two variables $\delta_1\delta_2$ and $\tau_1 + \tau_2$ and (b) oscillation amplitude of the self-excited system as a function of the two variables $\delta_1\delta_2$ and $\tau_1 + \tau_2$ when $\sigma = 0.0$.

Based on the above deduction, the stability chart of the controlled self-excited system in terms of $\delta_1\delta_2$ and $\tau_1 + \tau_2$ has been obtained using Equation (28) at nine different values of the excitation frequency $\Omega = \omega + \sigma$, $\sigma = -0.5, -0.4, -0.2, -0.1, 0, 0.1, 0.2, 0.4, 0.5$ as shown in Figure 19. It is clear from the figure that stable and unstable solution regions have been repeated periodically along $\tau_1 + \tau_2$ axis as predicted from Equation (32) and Figure 18a. In addition, Figure 19 demonstrate that the variation of the system excitation

frequency from $\Omega = \omega - 0.5$ as in Figure 19a to $\Omega = \omega + 0.5$ as in Figure 19i has negligible influence on the topology of both the stable and unstable solution regions.

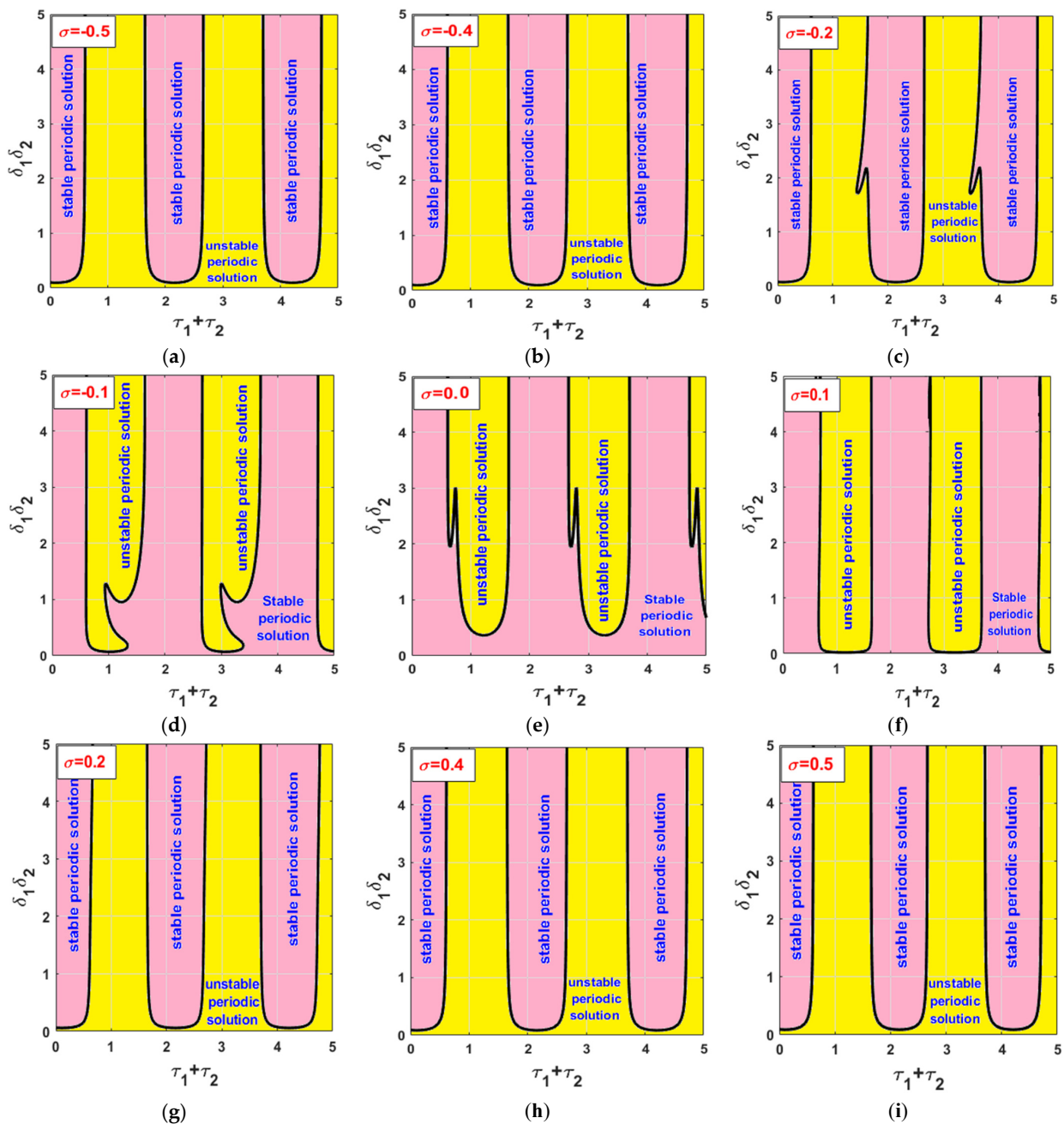


Figure 19. Stable and unstable periodic solution regions in $\tau - \delta$ plane at nine different values of the detuning parameter σ , where $\tau = \tau_1 + \tau_2$ and $\delta = \delta_1\delta_2$: (a) $\sigma = -0.5$, (b) $\sigma = -0.4$, (c) $\sigma = -0.2$, (d) $\sigma = -0.1$, (e) $\sigma = 0.0$, (f) $\sigma = 0.1$, (g) $\sigma = 0.2$, (h) $\sigma = 0.4$, (i) $\sigma = 0.5$.

To validate the accuracy of the obtained stability chart in Figure 19, let us investigate the system oscillation behaviors numerically at the two different values of the loop delays $\tau_1 + \tau_2 = 1$ (i.e., lie within the unstable solution region) and $\tau_1 + \tau_2 = 2$ (i.e., lie within the stable solution region). Accordingly, the controlled self-excited system vibration amplitude (a) has been plotted in $\sigma - \delta_1\delta_2$ plane using Equation (28) at $\tau_1 + \tau_2 = 2$ as shown in Figure 20a. It is clear from the figure that the system exhibits stable periodic solution along σ -axis. In addition, the steady-state oscillation amplitude is a monotonic decreasing function of $\delta_1\delta_2$. Moreover, to validate Figure 20a numerically, Equation (28) has been

solved as an implicit equation in terms of a and σ with fixing $\tau_1 + \tau_2 = 2$ at three different values of $\delta_1\delta_2$ (i.e., when $\delta_1\delta_2 = 1.0, 2.0, 3.0$) as shown in Figure 20b–d, respectively. It is clear from Figure 20b–d the excellent correspondence between the analytical and numerical solutions. It is worth mentioning that the numerical solution of the delayed dynamical system (i.e., Equations (2) and (3) when $\tau_1 + \tau_2 = 2$) has been obtained using the DDE23 MATLAB solver [41]. To simulate the transient and steady-state vibration of the time-delayed controlled system when increasing $\delta_1\delta_2$ online, the system time-response and phase-plane trajectory has been illustrated according to Figure 20 at $\sigma = 0$ in Figure 21 when increasing $\delta_1\delta_2$ from 1.0 to 2.0 at the time instance $t = 100$, and then increasing $\delta_1\delta_2$ from 2.0 to 3.0 at $t = 200$. It is clear from the figure that the time-delayed system oscillates periodically, where its vibration amplitude is a monotonic decreasing function of $\delta_1\delta_2$.

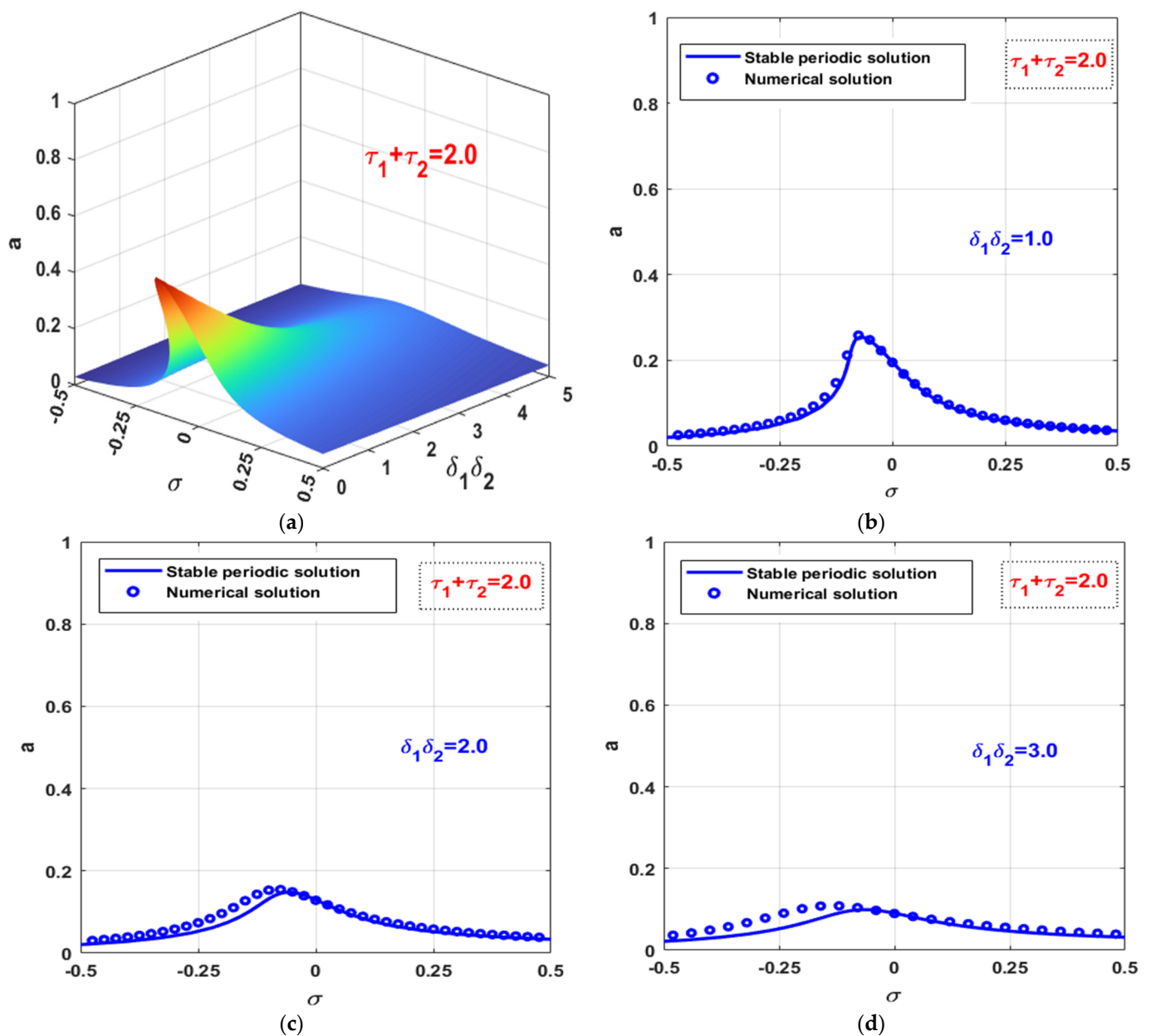


Figure 20. (a) Three-dimensional visualization of the steady-state vibration amplitude as a function of the two variables σ and $\delta_1\delta_2$ when $\tau_1 + \tau_2 = 2.0$, and (b–d) the self-excited system frequency-response curves when $\tau_1 + \tau_2 = 2.0$ at $\delta_1\delta_2 = 1.0, 2.0$, and 3.0 , respectively.

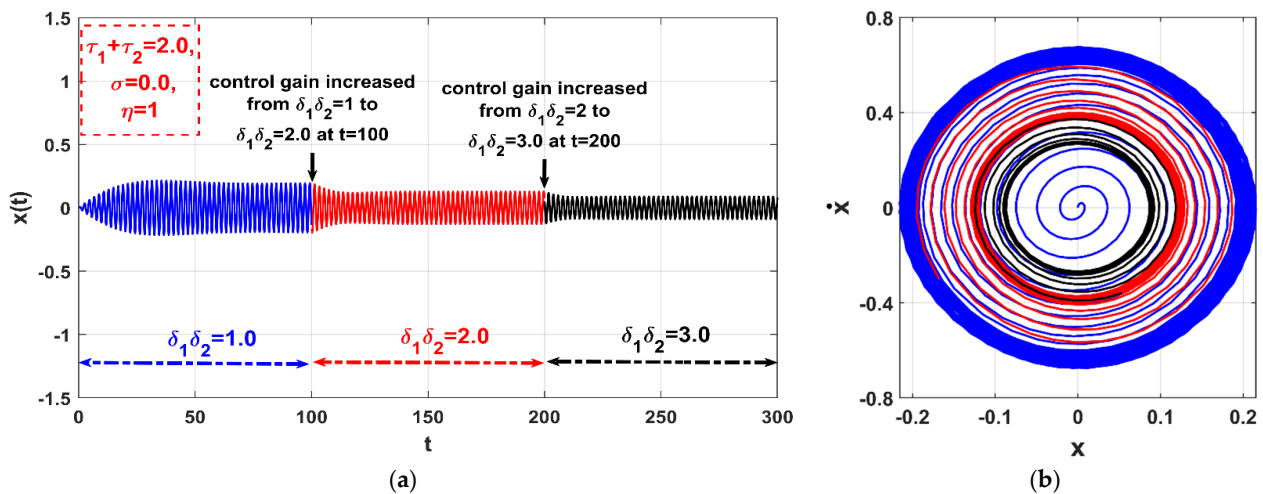


Figure 21. The temporal oscillations and the corresponding phase trajectories of the self-excited system according to Figure 20 at $\tau_1 + \tau_2 = 2.0$, $\sigma = 0$ when increasing $\delta_1\delta_2$ online from 1 to 2 at $t = 100$, and then from 2 to 3 at $t = 200$: (a) temporal oscillations of the self-excited system and (b) the corresponding phase trajectory.

On the other hand, the vibration amplitude (a) of the time-delayed system has been plotted in $\sigma - \delta_1\delta_2$ plane using Equation (28) according to the stability chart given in Figure 19 when $\tau_1 + \tau_2 = 1.0$ as shown in Figure 22a. In addition, Equation (28) has been solved as an implicit equation in the two variables a and σ when fixing $\tau_1 + \tau_2 = 1.0$ at three different values of $\delta_1\delta_2$ (i.e., when $\delta_1\delta_2 = 1.0, 2.0, 3.0$) as in Figure 22b–d. It is clear from Figure 22 in general that the controlled system has lost its stability along σ -axis when the time delay was selected to be within the unstable solution region of the stability chart given in Figure 19. To validate the accuracy of the analytical response curves in Figure 22b–d, the time-delayed system temporal oscillation and the corresponding phase trajectory have been illustrated in Figure 23 via solving Equations (2) and (3) numerically using DDE23 MATLAB solver at $\sigma = 0$, $\tau_1 + \tau_2 = 1.0$ with increasing $\delta_1\delta_2$ from 1.0 to 2.0 at $t = 100$, and then increasing $\delta_1\delta_2$ from 2.0 to 3.0 at $t = 200$. It is clear from Figure 23 that the system performs a quasi-periodic motion that is monotonically increasing function of $\delta_1\delta_2$.

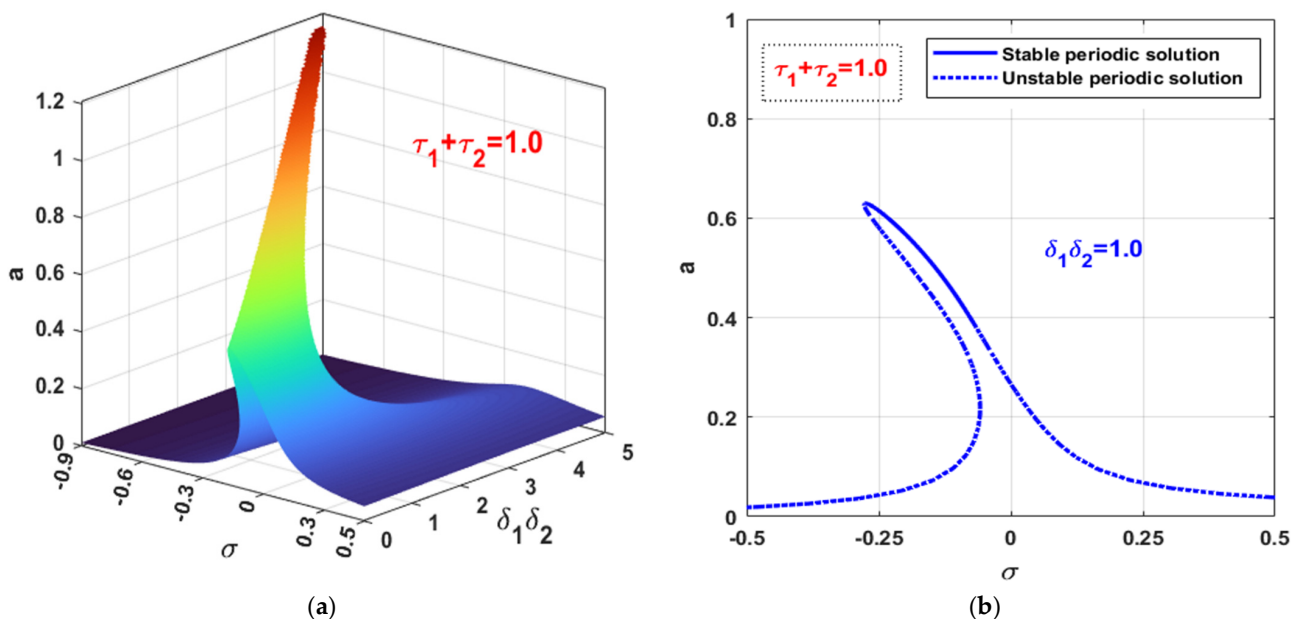


Figure 22. Cont.

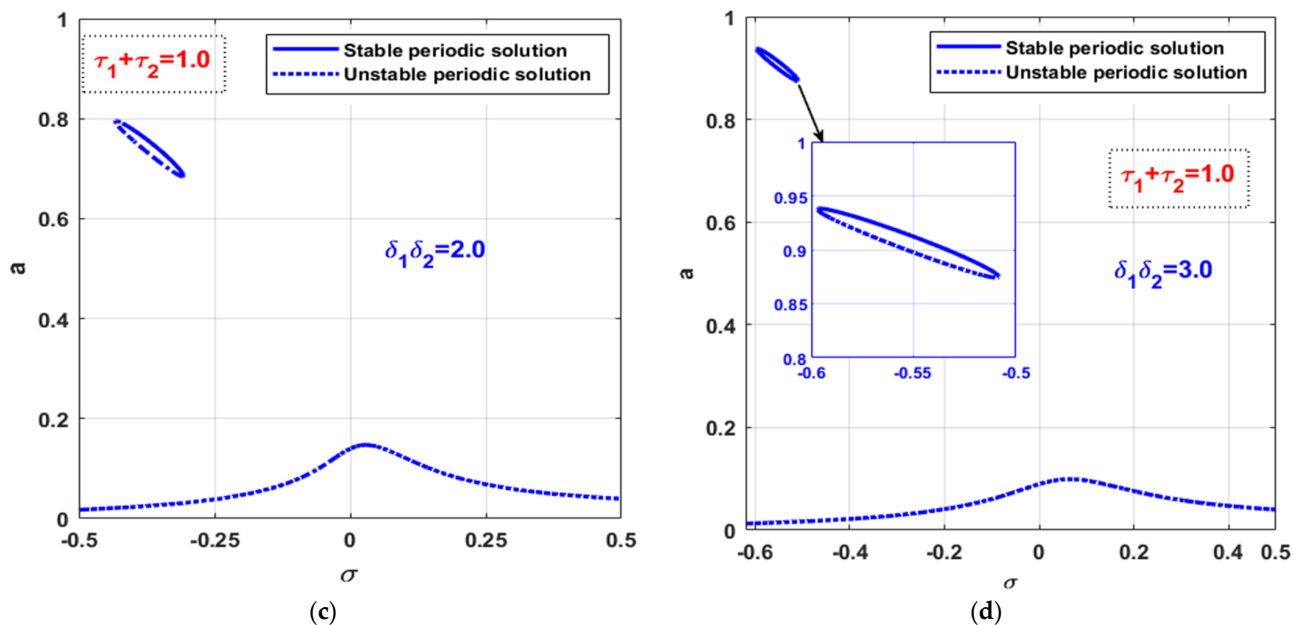


Figure 22. (a) Three-dimensional visualization of the steady-state vibration amplitude as a function of the two variables σ and $\delta_1\delta_2$ when $\tau_1 + \tau_2 = 1.0$, and (b–d) the self-excited system frequency-response curves when $\tau_1 + \tau_2 = 1.0$ at $\delta_1\delta_2 = 1.0, 2.0,$ and 3.0 , respectively.

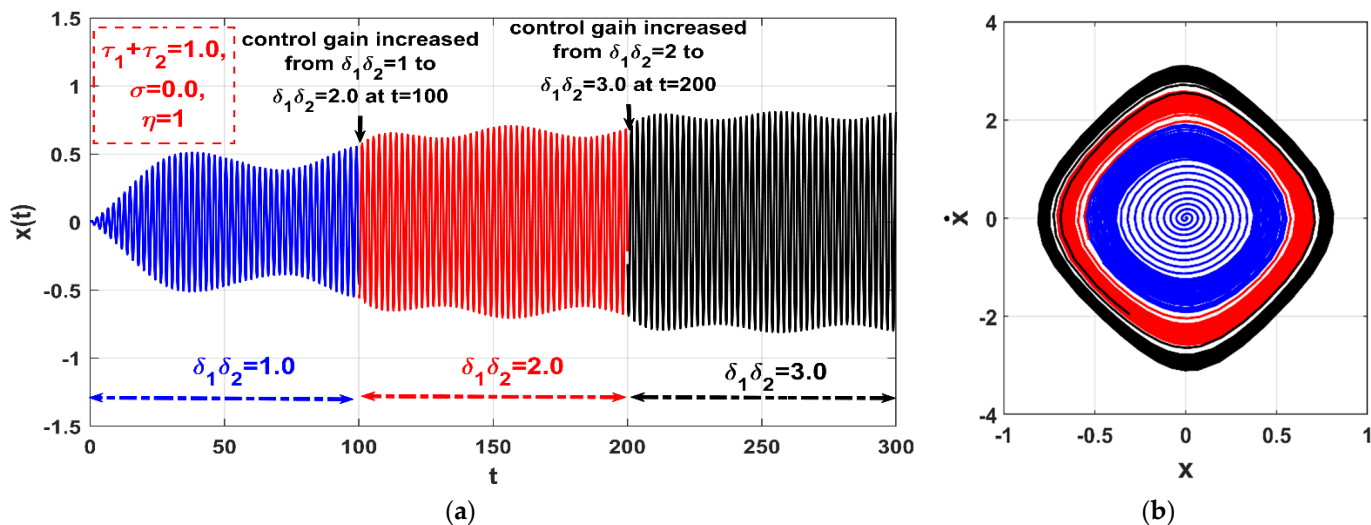


Figure 23. The temporal oscillations and the corresponding phase trajectories of the self-excited system according to Figure 22 at $\tau_1 + \tau_2 = 1.0, \sigma = 0$ when increasing $\delta_1\delta_2$ online from 1 to 2 at $t = 100$, and then from 2 to 3 at $t = 200$: (a) temporal oscillations of the self-excited system and (b) the corresponding phase trajectory.

4. Conclusions

Within this work, a time-delayed integral resonant controller has been proposed to stabilize the unstable motion and suppress the nonlinear oscillations of a nonlinear self-excited system for the first time. According to the suggested control strategy, the whole system dynamical model has been investigated using the asymptotic analysis, where the time delays of the control loop have been considered. The slow-flow nonlinear autonomous differential equations that govern the oscillation amplitude and the phase angle of the controlled self-excited system have been derived. In addition, the corresponding frequency-response equation that governs the system’s steady-state oscillation amplitude as a function of the different system and control parameters has been extracted. Using the obtained

frequency-response equation, the self-excited system bifurcation behaviors have been studied in the two- and three-dimensional spaces. The influences of the control gain, feedback gain, and loop delays on the system dynamics have been explored. Based on the introduced study, the following important remarks can be concluded:

1. The uncontrolled self-excited system can perform one of two bounded motions, which are the periodic and quasi-periodic vibrations;
2. The uncontrolled self-excited system can oscillate with one of four oscillation modes depending on the excitation frequency, which are mono-stable periodic oscillations, bi-stable periodic oscillations, periodic and quasi-period oscillations, and quasi-periodic oscillations only;
3. The coupling of an integral resonant controller to a self-excited system can stabilize the unstable motion and eliminate the system bifurcation behaviors;
4. The vibration suppression efficiency of the proposed control law (i.e., IRC) is proportional to the mathematical multiplication of both the feedback and control signals gains (i.e., $\delta_1 \times \delta_2$), and inversely proportional to the square of the internal loop feedback gain (i.e., η) when the time delay is neglected;
5. The existence of time delay (i.e., $\tau_1 \geq 0$ and $\tau_2 \geq 0$) in the control loop may improve or degrade the vibration suppression efficiency of the integral resonant controller depending on the magnitude of their summation (i.e., $\tau_1 + \tau_2$);
6. To get the best vibration suppression efficiency of the integral resonant controller when the loop delay is neglected, the controller parameters (δ_1 , δ_2 , and η) should be selected in such a way that maximizes the equivalent damping function $\mu_c(\delta_1, \delta_2, \eta)$;
7. To get the best vibration suppression efficiency of the time-delayed integral resonant controller, the controller parameters (δ_1 , δ_2 , η , τ_1 and τ_2) should be selected in such a way that maximizes the equivalent damping function $\mu_{c\tau}(\delta_1, \delta_2, \eta, \tau_1, \tau_2)$.

Author Contributions: Conceptualization, N.A.S., J.A. and M.S.M.; Data curation, N.A.S.; Formal analysis, N.A.S.; Funding acquisition, J.A. and M.S.M.; Investigation, N.A.S., J.A. and M.S.M.; Methodology, N.A.S. and M.S.M.; Project administration, N.A.S., J.A. and M.S.M.; Resources, N.A.S., and M.A.A.; Software, N.A.S. and J.A.; Supervision, N.A.S., J.A. and M.S.M.; Validation, N.A.S. and M.S.M.; Visualization, N.A.S. and M.A.A.; Writing—original draft, N.A.S. and J.A.; Writing—review & editing, N.A.S., J.A. and M.S.M. All authors have read and agreed to the published version of the manuscript.

Funding: This research was funded by Researchers Supporting Project, Taif University, Taif, Saudi Arabia under grant number TURSP-2020/160. This work was also supported by the National Science Centre, Poland under grant number OPUS 14 No. 2017/27/B/ST8/01330.

Institutional Review Board Statement: Not applicable.

Informed Consent Statement: Not applicable.

Data Availability Statement: Not applicable.

Acknowledgments: The authors would like to thank Taif University, where this work was supported by the Taif University Researchers Supporting Project number (TURSP-2020/160), Taif, Saudi Arabia.

Conflicts of Interest: The authors declare no potential conflict of interest concerning the research, authorship, and/or publication of this article.

List of Symbols

x, \dot{x}, \ddot{x}	The transversal displacement, velocity, and acceleration of the self-excited system.
y, \dot{y}	The displacement and velocity of the time-delayed integral resonant controller.
μ	The self-excited system linear damping parameter.
ω	The self-excited system linear natural frequency.
α	Cubic nonlinear stiffness coefficient of the self-excited system.
β	Cubic nonlinear damping coefficient of the self-excited system.
γ	Dimensionless disk eccentricity of the six-pole rotor active magnetic bearing system.

f	Excitation force amplitude.
λ	Constant depending on the system geometry.
Ω	Excitation force angular frequency.
δ_1	Control signal gain.
δ_2	Feedback signal gain.
H	Internal loop feedback gain of the controller.
τ_1, τ_2	Time delays of the closed-loop control system.
μ_c	Linear damping coefficient of the controlled self-excited system when $\tau_1, \tau_2 = 0$.
$\mu_{c\tau}$	Linear damping coefficient of the controlled self-excited system when $\tau_1, \tau_2 > 0$.
a	The steady-state oscillation amplitude of the self-excited system.
ϕ	The steady-state phase angle of the self-excited system.

References

- Abadi, A. Nonlinear Dynamics of Self-Excitation in Autoparametric Systems. Ph.D. Thesis, University of Utrecht, Utrecht, The Netherlands, 2003.
- Strogatz, S.H. *Nonlinear Dynamics and Chaos*; CRC Press: Boca Raton, FL, USA, 2018.
- Warminski, J. Nonlinear dynamics of self-, parametric, and externally excited oscillator with time delay: Van der Pol versus Rayleigh models. *Nonlinear Dyn.* **2020**, *99*, 35–56. [\[CrossRef\]](#)
- Tondl, A.; Ruijgrok, T.; Verhulst, F.; Nabergoj, R. *Autoparametric Resonance in Mechanical Systems*; Cambridge University Press: New York, NY, USA, 2000.
- Szabelski, K.; Warminski, J. The self-excited system vibrations with the parametric and external excitations. *J. Sound Vib.* **1995**, *187*, 595–607. [\[CrossRef\]](#)
- Szabelski, K.; Warminski, J. The parametric self-excited non-linear system vibrations analysis with the inertial excitation. *Int. J. Non-Linear Mech.* **1995**, *30*, 179–189. [\[CrossRef\]](#)
- Szabelski, K.; Warminski, J. Vibrations of a non-linear self-excited system with two degrees of freedom under external and parametric excitation. *Nonlinear Dyn.* **1997**, *14*, 23–36. [\[CrossRef\]](#)
- El-Budway, A.A.; Nasr El-Deen, T.N. Quadratic nonlinear control of a self-excited oscillator. *J. Vib. Control* **2007**, *13*, 403–414. [\[CrossRef\]](#)
- Jun, L.; Xiaobin, L.; Hongxing, H. Active nonlinear saturation-based control for suppressing the free vibration of a self-excited plant. *Commun. Nonlinear Sci. Numer. Simul.* **2010**, *15*, 1071–1079. [\[CrossRef\]](#)
- Warminski, J.; Cartmell, M.P.; Mitura, A.; Bochenski, M. Active vibration control of a nonlinear beam with self-and external excitations. *Shock. Vib.* **2013**, *20*, 1033–1047. [\[CrossRef\]](#)
- Abdelhafez, H.; Nassar, M. Effects of time delay on an active vibration control of a forced and Self-excited nonlinear beam. *Nonlinear Dyn.* **2016**, *86*, 137–151. [\[CrossRef\]](#)
- Macarri, A. Vibration control for the primary resonance of a cantilever beam by a time delay state feedback. *J. Sound Vib.* **2003**, *259*, 241–251. [\[CrossRef\]](#)
- Alhazza, K.A.; Nayfeh, A.H.; Daqaq, M.F. On utilizing delayed feedback for active-multimode vibration control of cantilever beams. *J. Sound Vib.* **2009**, *319*, 735–752. [\[CrossRef\]](#)
- Alhazza, K.A.; Majeed, M.A. Free vibrations control of a cantilever beam using combined time delay feedback. *J. Vib. Control* **2011**, *18*, 609–621. [\[CrossRef\]](#)
- Peng, J.; Zhang, G.; Xiang, M.; Sun, H.; Wang, X.; Xie, X. Vibration control for the nonlinear resonant response of a piezoelectric elastic beam via time-delayed feedback. *Smart Mater. Struct.* **2019**, *28*, 095010. [\[CrossRef\]](#)
- Daqaq, M.F.; Alhazza, K.A.; Qaroush, Y. On primary resonances of weakly nonlinear delay systems with cubic nonlinearities. *Nonlinear Dyn.* **2011**, *64*, 253–277. [\[CrossRef\]](#)
- Zhao, Y.Y.; Xu, J. Using the delayed feedback control and saturation control to suppress the vibration of the dynamical system. *Nonlinear Dyn.* **2012**, *67*, 735–753. [\[CrossRef\]](#)
- Saeed, N.A.; El-Ganini, W.A. Utilizing time-delays to quench the nonlinear vibrations of a two-degree-of-freedom system. *Meccanica* **2017**, *52*, 2969–2990. [\[CrossRef\]](#)
- Saeed, N.A.; El-Ganini, W.A. Time-delayed control to suppress the nonlinear vibrations of a horizontally suspended Jeffcott-rotor system. *Appl. Math. Model.* **2017**, *44*, 523–539. [\[CrossRef\]](#)
- Saeed, N.A.; Moatimid, G.M.; Elsabaa, F.M.F.; Ellabban, Y.Y.; El-Meligy, M.A.; Sharaf, M. Time-delayed nonlinear feedback controllers to suppress the principal parameter excitation. *IEEE Access* **2020**, *8*, 226151–226166. [\[CrossRef\]](#)
- Saeed, N.A.; Moatimid, G.M.; Elsabaa, F.M.F.; Ellabban, Y.Y. Time-delayed control to suppress a nonlinear system vibration utilizing the multiple scales homotopy approach. *Arch. Appl. Mech.* **2021**, *91*, 1193–1215. [\[CrossRef\]](#)
- Xu, J.; Chung, K.W.; Zhao, Y.Y. Delayed saturation controller for vibration suppression in stainless-steel beam. *Nonlinear Dyn.* **2010**, *62*, 177–193. [\[CrossRef\]](#)
- Saeed, N.A.; Eissa, M.; El-Ganini, W.A. Nonlinear time delay saturation-based controller for suppression of nonlinear beam vibrations. *Appl. Math. Model.* **2013**, *37*, 8846–8864. [\[CrossRef\]](#)

24. Saeed, N.A.; El-Gohary, H.A. Influences of time-delays on the performance of a controller based on the saturation phenomenon. *Eur. J. Mech.-A/Solids* **2017**, *66*, 125–142. [[CrossRef](#)]
25. Eissa, M.; Kamel, M.; Saeed, N.A.; El-Ganaini, W.A.; El-Gohary, H.A. Time-delayed positive-position and velocity feedback controller to suppress the lateral vibrations in nonlinear Jeffcott-rotor system. *Menoufia J. Electron. Eng. Res.* **2018**, *27*, 261–278. [[CrossRef](#)]
26. Diaz, I.M.; Pereira, E.; Reynolds, P. Integral resonant control scheme for cancelling human-induced vibrations in light-weight pedestrian structures. *Struct. Control Health Monit.* **2012**, *19*, 55–69. [[CrossRef](#)]
27. Al-Mamun, A.; Keikha, E.; Bhatia, C.S.; Lee, T.H. Integral resonant control for suppression of resonance in piezoelectric micro-actuator used in precision servomechanism. *Mechatronics* **2013**, *23*, 1–9. [[CrossRef](#)]
28. Omid, E.; Mahmoodi, S.N. Sensitivity analysis of the nonlinear integral positive position feedback and integral resonant controllers on vibration suppression of nonlinear oscillatory systems. *Commun. Nonlinear Sci. Numer. Simulat.* **2015**, *22*, 149–166. [[CrossRef](#)]
29. Omid, E.; Mahmoodi, S.N. Nonlinear vibration suppression of flexible structures using nonlinear modified positive position feedback approach. *Nonlinear Dyn.* **2015**, *79*, 835–849. [[CrossRef](#)]
30. Omid, E.; Mahmoodi, S.N. Nonlinear integral resonant controller for vibration reduction in nonlinear systems. *Acta Mech. Sin.* **2016**, *32*, 925–934. [[CrossRef](#)]
31. MacLean, J.D.J.; Sumeet, S.A. A modified linear integral resonant controller for suppressing jump phenomenon and hysteresis in micro-cantilever beam structures. *J. Sound Vib.* **2020**, *480*, 115365. [[CrossRef](#)]
32. Saeed, N.A.; Moatimid, G.M.; Elsabee, F.M.; Ellabban, Y.Y.; Elagan, S.K.; Mohamed, M.S. Time-Delayed Nonlinear Integral Resonant Controller to Eliminate the Nonlinear Oscillations of a Parametrically Excited System. *IEEE Access* **2021**, *9*, 74836–74854. [[CrossRef](#)]
33. Saeed, N.A.; Mohamed, M.S.; Elagan, S.K.; Awrejcewicz, J. Integral Resonant Controller to Suppress the Nonlinear Oscillations of a Two-Degree-of-Freedom Rotor Active Magnetic Bearing System. *Processes* **2022**, *10*, 271. [[CrossRef](#)]
34. Nayfeh, A. *Nonlinear Interactions, Analytical, Computational and Experimental Methods*; Wiley Series in Nonlinear Science; Wiley: New York, NY, USA, 2000.
35. Leniowska, L.; Mazan, D. MFC sensors and actuators in active vibration control of the circular plate. *Arch. Acoust.* **2015**, *40*, 257–265. [[CrossRef](#)]
36. Nayfeh, A.H. Resolving Controversies in the Application of the Method of Multiple Scales and the Generalized Method of Averaging. *Nonlinear Dyn.* **2005**, *40*, 61–102. [[CrossRef](#)]
37. Nayfeh, A.H.; Mook, D.T. *Nonlinear Oscillations*; Wiley: New York, NY, USA, 1995.
38. Slotine, J.-J.E.; Li, W. *Applied Nonlinear Control*; Prentice Hall: Englewood Cliffs, NJ, USA, 1991.
39. Yang, W.Y.; Cao, W.; Chung, T.; Morris, J. *Applied Numerical Methods Using Matlab*; John Wiley & Sons, Inc.: Hoboken, NJ, USA, 2005.
40. Ke-Hui, S.; Xuan, L.; Zhu, C.-X. The 0-1 test algorithm for chaos and its applications. *Chin. Phys. B* **2010**, *19*, 110510.
41. Shampine, L.F.; Thompson, S. Solving DDEs in MATLAB. *Appl. Numer. Math.* **2001**, *37*, 441–458. [[CrossRef](#)]